SANDIA REPORT
SAND2004-1642
Unlimited Release
Printed May 2004

Closed-Loop Biomass Co-firing in a Laboratory Reactor and in a Full-Scale Boiler

Linda G. Blevins, Sandia National Laboratories
Lee A. Jakeway, Hawaiian Commercial & Sugar Company
Bryan M. Jenkins & Robert B. Williams, University of California, Davis
Scott Q. Turn, Hawaii Natural Energy Institute

Prepared by
Sandia National Laboratories
Albuquerque, New Mexico 87185 and Livermore, California 94550

Sandia is a multiprogram laboratory operated by Sandia Corporation,
a Lockheed Martin Company, for the United States Department of Energy's
National Nuclear Security Administration under Contract DE-AC04-94AL85000.

Sandia National Laboratories

Issued by Sandia National Laboratories, operated for the United States Department of Energy by Sandia Corporation.

Available to DOE and DOE contractors from
U.S. Department of Energy
Office of Scientific and Technical Information
P.O. Box 62
Oak Ridge, TN 37831

Telephone: (865)576-8401
Facsimile: (865)576-5728
E-Mail: reports@adonis.osti.gov
Online ordering: http://www.osti.gov/bridge

Available to the public from
U.S. Department of Commerce
National Technical Information Service
5285 Port Royal Rd
Springfield, VA 22161

Telephone: (800)553-6847
Facsimile: (703)605-6900
E-Mail: orders@ntis.fedworld.gov
Online order: http://www.ntis.gov/help/ordermethods.asp?loc=7-4-0#online

Contents

List of Tables

List of Figures

Abstract

Co-firing tests were conducted in a pilot-scale reactor at Sandia National Laboratories and in a boiler at the Hawaiian Commercial & Sugar factory at Puunene, Hawaii. Combustion tests were performed in the Sandia Multi-Fuel Combustor using Australian coal, whole fiber cane including tops and leaves processed at three different levels (milled only, milled and leached, and milled followed by leaching and subsequent milling), and fiber cane stripped of its tops and leaves and heavily processed through subsequent milling, leaching, and milling cycles. Testing was performed for pure fuels and for biomass co-firing with the coal at levels of 30% and 70% by mass. The laboratory tests revealed the following information: (1) The biomass fuels convert their native nitrogen into NO more efficiently than coal because of higher volatile content and more reactive nitrogen complexes. (2) Adding coal to whole fiber cane to reduce its tendency to form deposits should not adversely affect NO emissions. (3) Stripped cane does not offer a NO advantage over whole cane when co-fired with coal. During the field test, Sandia measured O_2, CO_2, CO, SO_2, and NO concentrations in the stack and gas velocities near the superheater. Gas concentrations and velocities fluctuated more during biomass co-firing than during coal combustion. The mean O_2 concentration was lower and the mean CO_2 concentration was higher during biomass co-firing than during coal combustion. When normalized to a constant exhaust O_2 concentration, mean CO concentration was higher and mean NO concentration was lower for biomass co-firing than for coal. The SO_2 concentration tracked the use of Bunker C fuel oil. When normalized by the amount of boiler energy input, the amounts of NO and SO_2 formed were lower during biomass co-firing than during coal combustion. The difference between NOx trends in the lab and in the field are most likely a result of less effective heat and mass transfer in the boiler. Particles were sampled near the superheater tube using an impaction probe and were analyzed using scanning electron microscopy. Particle loading appeared higher for biomass co-firing than for coal combustion, especially for the smaller particle diameters. Laser-induced breakdown spectroscopy (LIBS) was used to detect silicon, aluminum, titanium, iron, calcium, magnesium, sodium, and potassium concentrations near the superheater. LIBS provided an abundant amount of real-time information. The major constituents of the fuel ash (silicon and aluminum) were also the major measured inorganic constituents of the combustion products. The combustion products were enriched in sodium relative to the fuel ash during all tests, and they were enriched in potassium for the biomass co-firing tests. Alkali metals are enriched because compounds containing these elements are more readily releasable into the combustion products than refractory components that remain in large particles such as silicon, aluminum, and titanium. Relative to the measured deposit chemistry, the combustion flows were enriched in iron, sodium, and potassium, constituents that are known to form fumes laden with fine particles and/or vapors. The LIBS results yield insight into the deposition mechanism: Impaction of larger particles dominates over fume deposition. The present application of LIBS reveals its potential to provide real-time field information on the deposition propensity of different fuels and the effects of different fuels and boiler operating conditions.

1 Introduction

Hawaiian Commercial & Sugar Company (HC&S) has been growing cane to produce sugar for more than a century. The company uses bagasse, the fibrous residue left after the sugar extraction process, as a biomass boiler fuel to provide steam and electricity for the sugar factory. The excess electricity generated is sold to the local utility. Since sugar cane is seasonal, expensive fossil fuels such as coal and residual fuel oil must be purchased and used during the off season to allow year-round power generation.

In recent years, HC&S and other companies have begun looking for ways to maintain profits in the face of declining revenues from sugar production. One potentially profitable pathway is to use cane as a dedicated energy crop to produce biopower directly, bypassing the sugar-making process entirely. Another possibility is to use cane to produce new bioproducts such as fiberboard or ethanol. The biopower option will potentially decrease the HC&S fuel cost by displacing expensive fossil fuels not native to Maui. Additionally, the use of an alternative fuel will displace some of the bagasse currently burned in the boilers, making it available for other uses such as fiber board production. Furthermore, a cane that bypasses the sugar mill has the potential to be used as a feedstock for ethanol production in the future. Finally, well-known environmental benefits motivate the increased use of energy crops around the world.

With partial support from the U.S. Department of Energy, HC&S undertook a project to select, grow, and demonstrate the use of "fiber cane" as a closed-loop biomass fuel for power generation. Fiber cane is defined as a cane optimized for fiber recovery instead of sugar recovery. Fiber cane is more economical than sugar cane because it requires fewer soil inputs (fertilizer and water) and it has morphology suitable for forage chopping and harvesting. Additionally, fiber cane can be garnered in its entirety, with stalks, leaves, and tops all used for fuel. This is in contrast to the usual HC&S procedure of harvesting only the stalks and has the potential to reduce the amount of open field burning of leaves and tops.

In the ideal (and least expensive) case, fiber cane would be harvested, chopped, and injected into the boiler for direct combustion without further processing. In reality, fiber cane straight from the field will contain chemicals such as potassium that may cause slagging in the boiler superheater and convection passes or on the fuel bed. This is not a usual concern with bagasse partially because its alkali metals are heavily leached away during sugar extraction. Hence, fiber cane may require some level of processing before it is ready to combust. Processing adds cost, so it is desirable to find the minimum level of fuel handling that can be used. An additional way to minimize the risk of boiler problems is to co-fire the fiber cane with coal, although this raises other concerns such as a greater potential to form oxides of nitrogen (NOx). Both fuel processing and co-firing of fiber cane were examined by HC&S. A fiber cane variety (B52298) was grown and harvested, and full-scale co-firing was performed in January 2002.

Few papers addressing fundamental bagasse combustion have been published. The only archival literature review on the topic was published in 1977; since little scientific work had been done

with bagasse at the time, the review focused on cellulose chemistry (cellulose is a component of bagasse) and fire spread through fuel beds.[1] Several papers describe improvements made to practical large-scale bagasse-fired boilers to improve efficiency.[2-6] Computational models of varying complexity are being developed for bagasse combustion systems such as grate furnaces, suspension-fired boilers, and fluidized bed combustors.[7-10] These models rely on fundamental kinetic data measured for bagasse pyrolysis and oxidation under low and high heating rates[11-18] and on measured bagasse particle properties.[7,19-21] Two laboratory studies published in the mid-1980s addressed fundamental bagasse combustion. Stubington and Fenton studied the effect of bagasse particle type (e.g., loose and densified fibers and small and large compressed pellets) and observed clinker formation in cases where combustion temperatures were high.[22] Cundy and coauthors reported successful and complete combustion of pulverized bagasse in a specially-designed laboratory swirl burner.[23] To the present authors' knowledge, no papers have been published describing fundamental experiments on NOx formation during bagasse combustion, although a few applied papers have featured information on these topics.[2,6,24,25] Additionally, no papers demonstrating combustion of unprocessed or minimally processed cane have appeared, and there is a dearth of information about co-firing of bagasse or cane with coal.

In support of the co-firing demonstration project, laboratory-scale experiments were performed at Sandia National Laboratories with the objective of helping HC&S identify the least amount of processing and/or the ideal co-firing ratio necessary to minimize boiler damage and curtail emissions. Sandia also participated in the field demonstration of fiber cane co-firing in January 2002 by deploying a laser-based diagnostic along with several more conventional measurement techniques. The purpose of this report is to document the methods, results, and conclusions from the Sandia laboratory and field testing.

2 Sandia Multi-Fuel Combustor Measurements

Four cane-derived fuels and one Australian coal were burned in the Sandia MFC. All cane-derived fuels were hand-harvested from small plots of B52298 fiber cane planted at HC&S. Table 1 lists the fuels used and the processing methods employed, while Table 2 contains important fuel properties. All fuels were reduced in size to about 1 mm and air-dried to a moisture content of less than 10 % to facilitate their use in the MFC. A detailed comparison of the different fuels employed in this effort was previously published.[26]

Table 1. Summary of fuels for pilot scale testing. WC = whole cane; SC = stripped cane; U = unprocessed; M = Cuba-milled 4 times; L = leached, 10:1 water-to-fiber weight ratio

Fuel ID	Material	Forage Chopped	Initial Cuba Milling (4 passes)	Leaching	Second Cuba Milling (4 passes)
AC	Australian Coal				
WCU	Whole Cane	X			
WCM	Whole Cane	X	X		
WCMLM	Whole Cane	X	X	X	X
SCMLM	Stripped Cane	X	X	X	X

Table 2. Properties of MFC test fuels.

	AC	WCU	WCM	WCMLM	SCMLM
Higher Heating Value (MJ/kg, dry ash free)	34.1	19.3	20.9	19.5	19.2
As-fired Moisture (% wet basis)	6.95	8.63	8.42	8.18	7.54
Proximate Analysis (% dry matter)					
Fixed Carbon	44.5	14.4	14.6	13.5	12.4
Volatiles	41.0	77.4	79.2	81.7	85.7
Ash	14.5	8.19	6.27	4.82	1.94
Ultimate Analysis (% dry matter)					
C	68.3	45.5	47.4	47.7	49.0
H	5.14	5.45	5.68	5.74	5.85
O (by difference)*	9.90	39.9	40.0	41.2	42.9
N	1.49	0.62	0.51	0.44	0.29
S	0.59	0.30	0.16	0.05	0.04
Ash Elemental Analysis (% ash, 600°C)					
SiO2	59.3	50.3	68.0	82.4	74.0
Al2O3	30.6	3.30	2.13	2.13	2.25
TiO2	1.71	0.53	0.27	0.31	0.39
Fe2O3	2.93	2.66	1.74	1.63	2.38
CaO	1.28	3.25	2.43	2.48	2.17
MgO	1.07	4.82	2.99	1.89	2.56
Na2O	0.91	0.83	0.58	0.46	0.95
K2O	0.65	22.4	12.5	4.04	6.90
P2O5	0.20	4.01	4.12	8.39	4.32
SO3	0.50	6.79	3.80	0.79	1.27
Cl	0.05	5.58	0.29	0.04	0.12
CO2	0.01	0.05	0.17	0.17	0.29

*Accounts for C, Cl, and S also included in ash.

2.1 Methods

Experiments were performed using the Sandia Multi-Fuel Combustor (MFC), a 15-cm diameter, 4.2-m long, silicon carbide, turbulent down-flow reactor.[27-29] The reactor consists of seven independently heated 0.6-m long sections. For the present tests, exhaust gases were continuously extracted from the seventh (bottom) section of the reactor using a 110 °C heated probe and sampling line. Chemiluminescent and paramagnetic analyzers were used to analyze for NOx and O_2 concentrations, respectively, just after the sample was cooled for water removal.

The MFC was operated with a wall temperature setting for each section of 1100 °C. In practice, the wall temperature can vary, especially in the upper two sections of the reactor. The upper sections can either be cooler than 1100 °C as a result of cold reactant heat transfer or warmer than 1100 °C owing to combustion heat release. This behavior depends on the rates of air and fuel flow into the reactor, but it was not documented as part of the present work.

Each biomass fuel in Table 1 was thoroughly mixed with coal at as-fired mass percentages of 0% (pure coal), 30%, 70%, and 100% (pure biomass). The as-fired mass percentages approximately equal the dry mass percentages since all fuels contained 7-9% moisture. For each fuel mixture, a single screw feeder was calibrated using a receptacle and stopwatch. MFC combustion tests were performed for each mixture. Primary air preheated to 500°C was injected into the first (top) reactor section. Additionally, 25°C transport air conveyed the solid fuels into the same reactor section. The rate of cold transport air flow was about 30% by mass of the total rate of air flow. The rates of primary and transport air flow were estimated using mass flow meters.

For each fuel, the rate of air flow into the reactor was held constant, while the rate of fuel flow was varied to obtain target dry exhaust O_2 concentrations between 0% and 15% by volume. Each O_2 concentration was maintained for several minutes until the NOx concentration achieved a steady state value. The total rate of air flow was predicted assuming complete conversion based on the rate of fuel flow, the fuel composition, and the measured exhaust O_2 concentration.

Table 3. Important parameters determining operating conditions during MFC tests. The number after the fuel ID indicates the mass percentage of biomass in the mixture.

Fuel ID	Air Meter Readings (g/min)	Predicted Air Flow (g/min)	Fuel Feeder Calibration Range (g/min)	Measured Fuel Flow Range (g/min)
AC100	990	730	28-71	32-78
WCU100	990	840	90-151	32-142
WCU30 (discarded)	900	320	90-157	16-38
WCU70	970	1100	115-211	49-172
WCM100	940	1050	47-131	45-136
WCM30 (discarded)	830	390	77-180	21-55
WCM70	940	1050	69-134	52-165
WCMLM100	920	1000	50-145	55-153
WCMLM30	830	880	84-136	41-110
WCMLM70	950	1040	73-170	60-155
SCMLM100	950	1200	90-157	56-180
SCMLM30	820	980	75-170	39-122
SCMLM70	950	1040	69-124	39-155

For each fuel, Table 3 shows the air meter reading (the approximate rate of flow based on the sum of the primary and transport air meter readings), the average rate of predicted air flow, the range for which the fuel feeder was calibrated, and the range of fuel flow rates employed. The table shows that, for two of the tests (WCU30 and WCM30), the predicted rates of air flow are

much lower than the estimated rates and the range of fuel flow rates falls well below the range of fuel feeder calibration. Thus, the results from the WCU30 and WCM30 tests were discarded.

The theoretical heat release rate, the product of the fuel mass flow rate and the higher heating value of the fuel, was kept relatively constant independent of fuel type for a given exhaust O_2 concentration. Figure 1 depicts the variation of this parameter for all experiments. The heat release rate varied approximately linearly from 47 ± 9 kW at 0% O_2 to 14 ± 4 kW at 15% O_2. Heat release rate was thus constant to within $\pm$ 20% for each exhaust O_2 concentration. Figure 2 depicts the variation of the approximate reactor residence time for all experiments. The residence time was constant to within $\pm$ 20% of the mean of 1.1 s for all fuels except for pure coal. The coal combustion reactants and products had a longer residence time of 1.5 s. The relatively constant heat release rate and residence time for a given O_2 concentration provide justification for comparing NOx results for different fuels at constant O_2 concentrations.

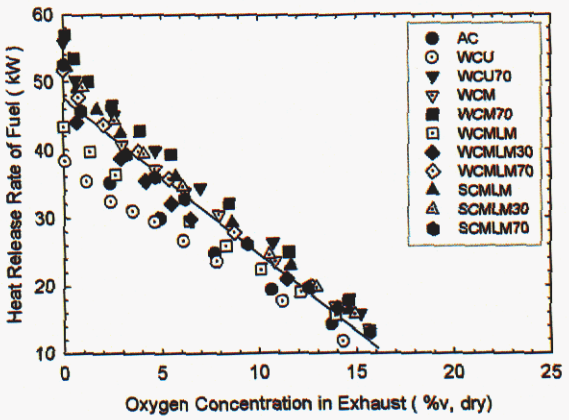

Figure 1. Range of heat release rates, calculated from measured rate of fuel flow and higher heating value, as a function of O_2 concentration for all MFC tests.

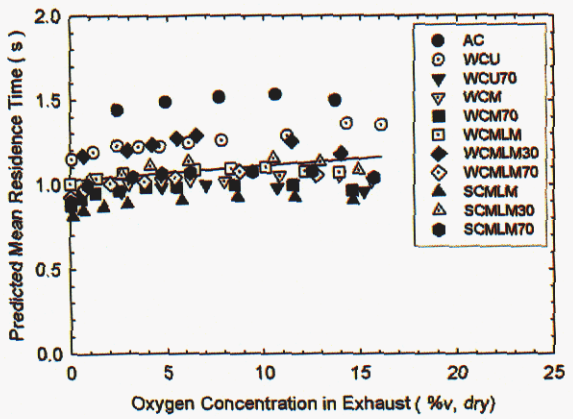

Figure 2. Range of reactor residence times, estimated using the measured rate of fuel flow, the predicted rate of air flow, and the reactor geometry, as a function of exhaust O_2 concentration.

2.2 Results

2.2.1 Pure Fuels

Figure 3 depicts the emission indices of NOx (EINOx) as a function of O_2 concentration for the pure coal and pure biomass fuels. The emission index is defined as the mass of pollutant formed per unit mass of fuel burned. The NOx is assumed to appear entirely as NO for the EINOx calculation. For a given fuel, EINOx increases slightly and then remains constant or decreases as O_2 concentration increases. EINOx increases because the relative amount of O_2 available to oxidize the fuel nitrogen increases; eventually, either the lower heat release rate or the cooling associated with the diluent N_2 from the air may lower local temperatures and thus NOx formation rates. Coal has a higher EINOx (~6 g/kg at 8% O_2) than any of the biomass fuels. The EINOx for the whole cane fuels has a similar value (~4 g/kg at 8% O_2) regardless of processing level. The heavily processed stripped cane (SCMLM) has a lower EINOx (~2 g/kg at 8% O_2) than any of the whole cane fuels. On a mass basis, these trends in NO production are consistent with the mass-based fuel nitrogen concentrations in Table 2.

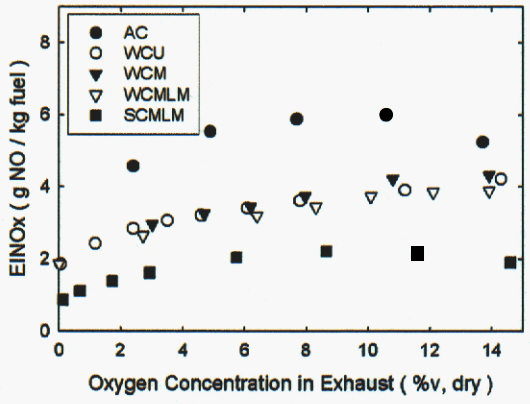

Figure 3. Emission indices of NOx for MFC testing with pure fuels.

As seen in Fig. 3, biomass fuels form less NOx than pure coal when the pollutant amounts are normalized by the mass of fuel consumed. However, biomass fuels have heating values lower than those of coal. To transfer an equivalent amount of thermal energy to steam in a boiler, more biomass than coal would be needed. To account for this effect, the "energy emission index," defined as the mass of pollutant formed per unit theoretical energy released, is examined in Fig. 4. The energy release rate is defined as the heat release rate in Fig. 1. In the figure, the coal and all of the whole cane fuels generate similar amounts of NOx (~0.21 g/MJ at 8% O_2). Only the stripped cane shows a lower value of Energy EINOx (~0.12 g/MJ at 8% O_2). Figure 4 shows that the presumed NOx benefit associated with using biomass is minimal for all but the most heavily processed fuel. To understand this trend, it is useful to examine the NO trends in yet a different way.

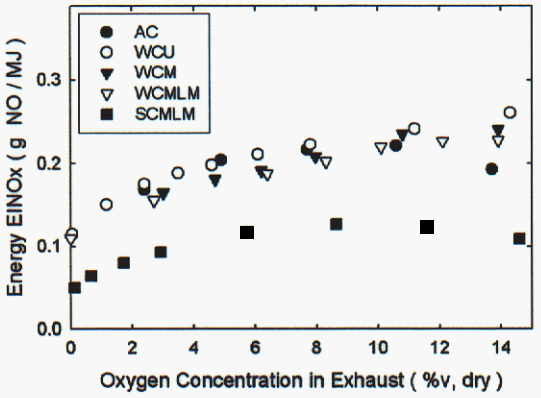

Figure 4. Energy-based emission indices of NOx for MFC testing with pure fuels.

Figure 5 depicts the percentage of fuel nitrogen converted to NOx as a function of exhaust O_2 concentration for each pure fuel. Surprisingly, the coal converts the lowest percentage of its nitrogen to NO (~20% conversion at 8% O_2). This happens in spite of the fact that the coal combustion products have the longest expected residence time in the reactor (Fig. 2). In comparison, the pure biomass fuels release 30% to 40% of their nitrogen as NO at 8% O_2. Hence, in the MFC, the biomass fuels appear to form NOx more readily than the coal. This can be explained by the fact that biomass forms very little char. Thus, nitrogen is released entirely during devolatilization. If oxygen is present, either from the combustion air or from the biomass volatiles themselves, NO is likely to form. On the other hand, coal releases some nitrogen as volatiles and retains some nitrogen in char. The char nitrogen can either form or reduce NO. Coal has more fixed carbon than biomass (Table 2) and is known to reduce NO on its surface during char oxidation.[30] Since biomass produces very little char, this effect is not expected for the cane-derived fuels of this study. An additional factor is that nitrogen exists in biomass in reactive amines, while it exists in coal attached to more stable ring structures.

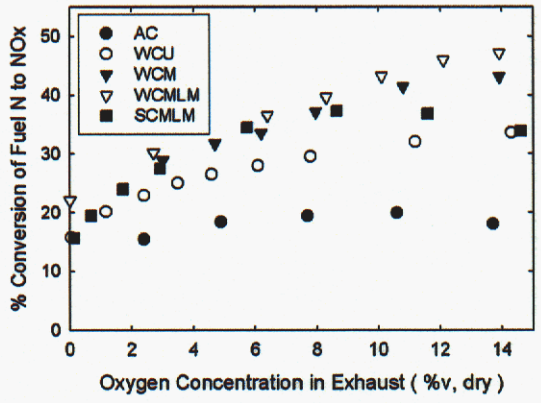

Figure 5. Conversion efficiency of N to NO for MFC testing with pure fuels.

In summary, Figs. 4-5 demonstrate that, in a pulverized combustion system such as the MFC, whole cane with any level of processing makes as much NOx as coal. To achieve a NOx benefit, one must strip the cane of tops and leaves and process it heavily to make a fuel like SCMLM. This is effectively the process experienced by normal bagasse before it is burned.

2.2.2 Co-firing

Figure 6 shows co-firing effects. Energy EINOx are depicted as a function of exhaust O_2 concentration for different co-firing levels for each biomass fuel. In Fig. 6, the differences between the amount of NOx produced during co-firing and that formed during pure biomass combustion are minimal. The only exception is the stripped cane (SCMLM): When fired alone, SCMLM fuel forms half as much NOx as when it is co-fired with coal in any amount. Hence, adding coal to the whole cane fuel to minimize deposition tendency should not affect NOx.

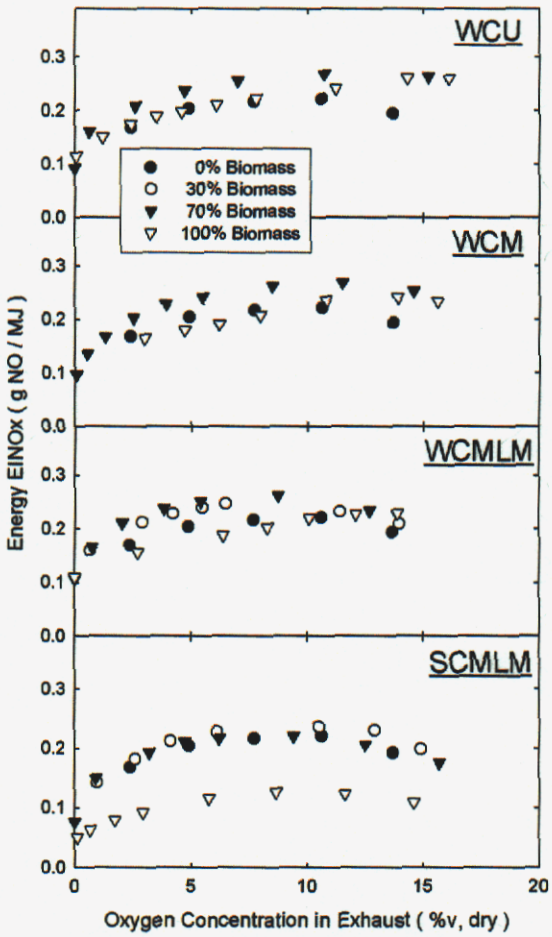

Figure 6. Energy based emission indices of NOx (NO equivalent) for MFC co-firing of biomass with Australian Coal (AC).

2.2.3 Differences between MFC and HC&S Boiler

The Sandia MFC is an entrained flow reactor. Fuels are reduced in size and dried before combustion. Devolatilization, volatiles combustion, and char reactions can take place sequentially or simultaneously throughout a cloud of suspended particles as the reactants and products traverse the reactor together. All of the fuel ash is entrained and emitted from the reactor.

For the HC&S stoker-fired grate boiler, on the other hand, fuels have relatively large particle sizes and are very wet when introduced. The grate boiler contains a moving fuel bed through which combustion air is passed. The fuel accumulates in piles on the bed. Drying and devolatilization take place on the bed, and volatiles combustion and char burnout occur in separate regions of the bed or downstream of the bed. Only the lightest ash and fuel particles and gaseous combustion products are entrained and carried toward the convection pass. Heavy ash falls off the grate as bottom ash and is not entrained into the flow.

Using the designations of Smoot[31], the MFC can be considered a pulverized fuel or suspended combustion device, while the HC&S boiler is designated a stoker or moving bed device. Accordingly, in the MFC, the fuel particle sizes are smaller, particle heating rates are higher, and peak particle temperatures are higher than in the HC&S boiler. The small particles (high surface area) and higher burning rates (rapid release of all fuel components) in the MFC enhance the rate of nitrogen release. In addition, oxidation of the released nitrogen occurs readily in the MFC because of the intermingling of air with fuel in the suspended combustion and the (generally) overall fuel-lean conditions. In contrast, nitrogen release in the HC&S boiler is limited by slow heat and mass transfer at the cooler surfaces of the larger fuel particles. Nitrogen oxidation to NO is limited in the HC&S boiler because of the more physically separated zones of devolatilization and combustion (i.e., air is available in limited supply in the devolatilization zone so some fuel nitrogen makes N_2).

An additional complication is that the MFC fuels are dried before combustion to facilitate feeding, while the HC&S boiler fuels are not. Also, fuels are fed continuously into the MFC while they are fed in batches into the HC&S boiler. The repeated fuel feeding-drying-devolatilizing-combusting cycle of the HC&S boiler leads to the well-known puffing instability of bagasse boilers.[8] This dynamic and somewhat sequential behavior is not present for the relatively dry fuels in the continuously fueled MFC.

Hence, the MFC should be considered an "ideal heat and mass transfer" case for the release of fuel constituents into the combustion space and their subsequent oxidation. This caveat must be considered when using the MFC gaseous pollutant results to guide fuel type, fuel processing, and/or co-firing choices for the HC&S boiler. Nonetheless, the basic research performed in the MFC can be useful as an idealized limit of combustion behavior.

2.3 Summary and Conclusions of Laboratory Tests

Combustion tests were performed in the Sandia MFC using Australian coal, whole fiber cane including tops and leaves processed at three different levels (milled only, milled and leached, and milled followed by leaching and subsequent milling), and fiber cane stripped of its tops and leaves and heavily processed through subsequent milling, leaching, and milling cycles. Testing was performed for pure fuels and for co-firing of biomass with the coal at levels of 30% and 70% by mass.

For pure coal and biomass fuels, NO was formed in amounts that trend with the relative fuel nitrogen concentrations. However, when NO amounts were normalized by fuel energy input, only the stripped cane produced less NO than the coal. The biomass fuels converted their native nitrogen into NO more efficiently than the coal, presumably because of higher volatiles content and more reactive nitrogen complexes. Independent of fuel processing level, co-firing whole cane with coal produced about as much NO per unit of energy input as that produced by pure coal or pure whole cane. Hence, adding coal to whole fiber cane to reduce its tendency to form deposits should not adversely affect NO emissions. Also, while stripping fiber cane of its tops and leaves reduces its tendency to form NOx when burned alone, stripped cane does not offer a NOx advantage over whole cane when co-fired with coal.

3 Sandia Field Measurements

This section highlights the application of multiple diagnostic tools featuring laser-induced breakdown spectroscopy (LIBS). LIBS was used for detecting multiple elements in the boiler during field testing, including sodium and potassium. The specific objectives of this section are to (1) demonstrate the use of LIBS as a real-time monitor of inorganic species in a boiler, and (2) use LIBS results to examine the differences in slagging potential between tests performed with different fuels. Major combustion products were also monitored by Sandia in the stack. Gas velocity was measured and particles were collected on impaction coupons. This section supports the overall project objective of determining the feasibility of using fiber cane as a closed-loop biomass fuel for power generation.

3.1 Introduction

Full scale testing was performed in a stoker-fired traveling grate boiler January 14-24, 2002. Figure 7 shows a boiler schematic. The demonstration consisted of three test segments (termed Test 1, Test 2, and Test 3) of about 60 hours apiece with different solid fuels. The boiler was operated such that the rate of steam flow remained constant at 45,360 kg/hr (100,000 lbm/hr) at 6.23 MPa (900 psig) and 400° C (750° F), resulting in about 10 MWe of power generated. Bunker C fuel oil was used in varying amounts at all times to maintain boiler stability. The boiler has three adjacent solid fuel feeders. For Test 1, the solid fuel in all three feeders was crushed Australian bituminous coal. For Test 2, bagasse was fed from each of the two outer feeders while coal was fed from the central feeder. For Test 3, a mixture of ~20% fiber cane by

weight with bagasse was fed from each of the two outer feeders while coal was fed from the central feeder. For Test 3, chopped fiber cane was stacked in the bagasse house in the desired proportion and mixed with bagasse by the reclaiming system before being conveyed to the boiler. Table 4 depicts estimates of the rates of fuel flow used during each test.

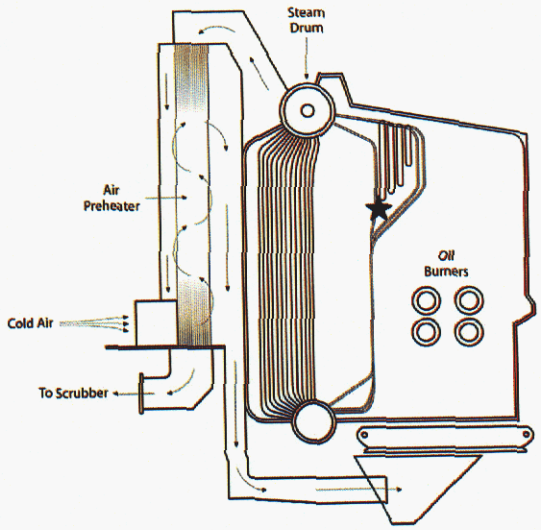

Figure 7. Schematic of HC&S boiler. The black star near the superheater tubes shows the approximate location of the Sandia measurements.

Table 4 Estimated fuel flow rates and percentages of thermal input

Test	Rate of Fuel Flow in kg/hr (lbm/hr) - % thermal			
	Coal	Bagasse	Fiber Cane	Bunker C Oil
1	5,169 (11,395) - 83%	---	---	626 (1,379) - 17%
2	2,520 (5,555) - 25%	16,905 (37,268) - 62%	---	755 (1,663) - 13%
3	3,551 (7,830) - 33%	13,033 (28,732) - 46%	2,774 (6,116) - 5%	1,012 (2,231) - 16%

Table 5 provides the ultimate, proximate, and ash analyses for the fuels used during testing. The abundance of metals such as Ti and Fe in the bagasse and fiber cane ash indicate the presence of adventitious soils in the fuels. Table 6 shows the rate of mass flow of elements into the boiler during Tests 1, 2, and 3 calculated using the values in Tables 4 and 5. The rates of flow in Table 5 are compared directly during data analysis because the boiler load (45,360 kg/hr steam at 6.23 MPa and 400° C) was kept constant for each test.

Table 5 Important results from fuel analyses

Ultimate Analysis of Parent Fuels (wt%, dry)				
	Coal	Bagasse	Fiber Cane	Fuel Oil
C	69.1	45.5	44.5	87.2
H	5.12	5.26	5.18	10.7
O (diff)	11.3	36.7	33.8	--
N	0.98	0.23	0.51	--
S	0.52	0.05	0.16	1.95
Cl	0.02	0.04	0.43	<0.01
Ash	13.1	12.4	15.7	0.04
Proximate Analysis of Parent Fuels (wt %, dry)				
	Coal	Bagasse	Fiber Cane	Fuel Oil
Moisture (wet %)	12	42	74	0.64
Ash (dry %)	13.1	12.4	15.7	0.04
Volatile (dry %)	46.0	77.4	71.6	--
Fixed C (dry %)	40.9	10.3	12.7	--
HHV, MJ/kg (dry)	28.4	16.9	16.8	43.4
Ash Analysis of Parent Fuels (wt%, dry)				
	Coal	Bagasse	Fiber Cane	Fuel Oil
SiO2	62.86	45.90	47.26	--
Al2O3	25.33	20.56	12.83	--
TiO2	1.68	3.77	2.67	--
Fe2O3	2.26	15.45	10.64	--
CaO	2.39	4.32	6.80	--
MgO	1.28	3.22	4.23	--
Na2O	1.07	0.96	1.76	--
K2O	0.41	1.68	7.29	--
P2O5	0.10	0.89	1.25	--
SO3	1.31	0.41	1.48	--
Cl	<0.01	<0.01	1.49	--
CO2	0.04	0.13	0.21	--

Table 6 Rates of mass flow of elements, ash, and moisture into the boiler

Estimated Rate of Mass Flow (kg/hr)			
	Test 1	Test 2	Test 3
C	3670	6330	6580
H	298	673	677
O (diff)	510	3590	3190
N	44.4	42.6	50.7
S	35.7	30.7	40.6
Cl	0.91	4.10	6.80
Moisture	645	8090	8430
Ash	594	1420	1400

3.2 Methods

3.2.1 Stack Gas Concentrations

Combustion gases were extracted from the stack and analyzed for O_2, CO_2, CO, NO, and SO_2 concentrations using a Horiba PG-250 stack gas analyzer. Gases were extracted from one of the ports used for traditional stack testing through an uncooled, 1.3 cm (0.5 in) diameter, blunt silicon carbide probe connected using a 0.4 L/min pump within the PG-250 analyzer. The gases were filtered to remove particles and then cooled and dried in an ice bath before analysis. Signals from the analyzer were recorded once every five seconds using a data acquisition system. Calibrations were performed once every 24 hours using certified span gases. Measured concentrations of CO, NO, and SO_2 were corrected to reflect those concentrations that would exist if the dry, volumetric concentration of O_2 were three percent. Representative four-hour corrected concentration traces for each test are presented and discussed. Because of a data acquisition system malfunction, only about two hours of data were collected during Test 2. Stack testing was also performed by a contractor using standard EPA methods during each of the three fuel test periods,[32] and some results are included here for comparison.

3.2.2 Gas Velocity

A water-jacketed S-type pitot tube (Dwyer series 160S) was used to determine the bulk gas velocity near the LIBS measurement location. The pitot tube, the tip of which is shown in Fig. 8(a), is a Darcy bi-directional probe manufactured from 0.79 cm stainless steel tubing. Velocity measurements were made for Tests 1, 2, and 3 at seven equally spaced insertion depths from 0.3 m (1 ft) to 2.1 m (7 ft) from the wall. At each measurement location, the pitot tube was rotated to different orientations representing 0°, 45°, 90°, 135°, and 180° from the vertical to find the dominant flow direction (defined as the direction for which differential pressure was maximum). The flow was found to move upward at 45° from the horizontal. One to two minutes of differential pressure data were collected at a rate of five data points per second using an electronic pressure transmitter at each insertion depth. The flow velocity is proportional to the square root of the ratio of the differential pressure and the gas density.[33] The gas was assumed to be air at 900°C, and the differential pressure was multiplied by the pitot tube flow coefficient of 0.84 in accordance with manufacturer recommendations. Pitot tube measurements were made for Test 1 on 1/17/02 from 4:00 p.m. until 5:30 p.m., for Test 2 on 1/20/02 from 11:00 p.m. to 12:30 a.m., and for Test 3 on 1/24/02 from 10:30 p.m. to 12:00 a.m.

3.2.3 Particle Impaction Sampling

Uncooled 2.5 cm (1 inch) diameter stainless steel impaction coupons fastened to the end of a metal rod, shown in Figure 8(b), were manually inserted into the flow for one-minute exposures during each test. The coupons were oriented normal to the dominant flow direction during sampling. Qualitative information about particle loading for each test was determined by

Scanning Electron Microscope (SEM) analysis of the coupons after the tests. A few representative images are provided in this report.

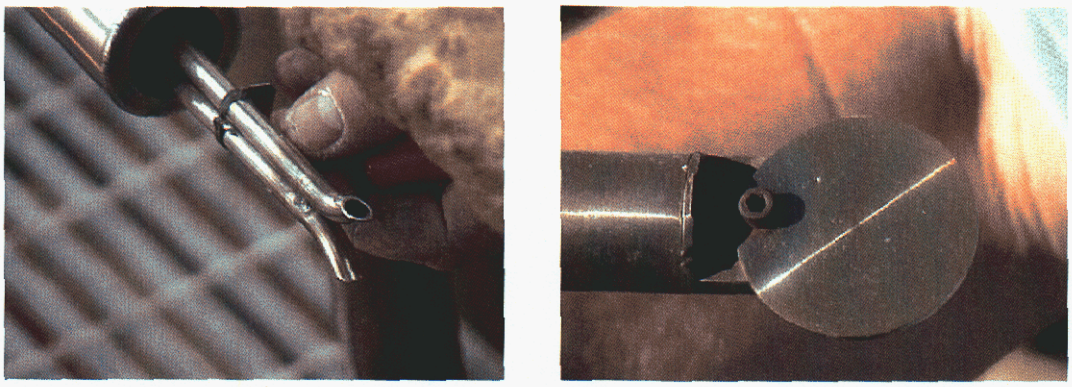

(a) (b)

Figure 8. Photographs of (a) tip of S-type pitot tube, and (b) impaction coupon after brief exposure near the superheater tubes.

3.2.4 Laser-Induced Breakdown Spectroscopy

For LIBS, shown schematically in Fig. 9, a laser beam is focused into a tiny volume (inside the boiler for the present work). The resulting optical breakdown creates a plasma containing atoms in electronically excited and ionic states. The spectrum of light emitted by the high-energy plasma is measured on a spectrometer. Elements are identified by the wavelength of their emitted light, and their concentrations are determined from the intensity of the light. LIBS as it is applied here cannot distinguish between particles and gases; the concentrations obtained herein are thus total concentrations in the particles and gases combined.

The specific LIBS unit deployed has evolved over the past several years, as reviewed in a recent publication and the references therein.[34] The system consists of a Q-switched Nd:YAG laser, a cooled and purged optics probe, an optical fiber, and detection hardware. The pulsed laser delivers 350 mJ of energy with a 10 ns pulse width. The laser is abutted to a rugged collection optics assembly and a stainless steel optics probe. The probe is 7.9 cm (3.1 in) in outer diameter and 91 cm (3 ft) long. Inside the probe, the beam is expanded to 12 mm and then focused to create a 2.5×10^{-4} cm^3 measurement volume spark using a 75 mm focal length, 50 mm diameter quartz lens. The plasma-emitted light is collected by the same lens, diverted by a mirror, focused onto a fiber optic, and delivered to the detection system. The use of fiber optics allowed the spectrometer and detector to be kept cool and clean in the control room. The detector consists of an intensified charge-coupled device camera coupled to an echelle spectrometer for light dispersion. This relatively new technology allows detection of ultraviolet, visible, and near-infrared light between 200 nm and 900 nm with high spectral resolution in a single measurement. The probe was inserted through a knife gate port installed in the boiler casing near the fourth bank of superheater tubes, as shown in Figs. 7 and 10.

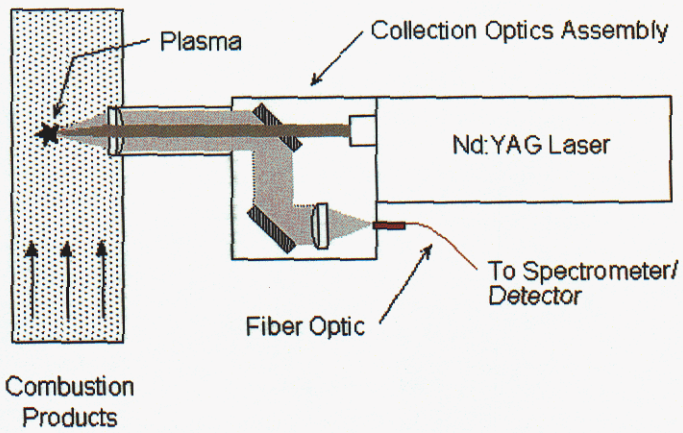

Figure 9. Schematic of LIBS system.

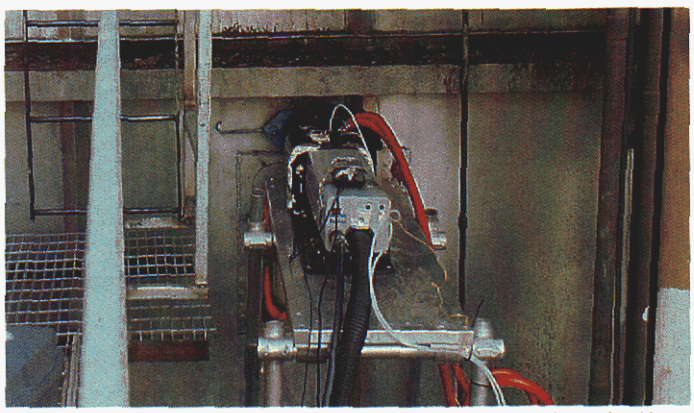
Figure 10. Photograph of LIBS laser with optical probe inserted into boiler wall.

Because the refractory wall is ≈30 cm (12 in) deep, the LIBS probe volume was positioned about 61 cm (2 ft) from the wall. The boiler duct is ≈610 cm (20 ft) wide at this location. The mean gas temperature measured using a thermocouple was ~900 °C for all three tests. Plant utility water was circulated through the probe water jacket at 10.4 L/min (2.8 gal/min). N_2 was used to purge the lens at a rate of flow of about 18 L/min.

Spectra were collected at 5 Hz with a delay time of 20 μs and a gate width of 50 μs. Spectra were ensemble averaged for 1000 shots, so each recorded spectrum represents about three minutes of data. It was found that the wavelength calibration of the spectrometer drifted over the course of several hours on a given day (see Jan. 20 and Jan. 22 results in Appendix B). The drift affected both the wavelength and the signal intensity in unrelated ways, so spectra could not be corrected. Hence, a procedure of performing spectrometer wavelength calibrations using a fiber-coupled Hg lamp once per hour was implemented. Further details about the LIBS system, the

field hardware, the optics, and the electronic settings are published elsewhere.[34] Typical spectra from each test are shown in Figure 11.

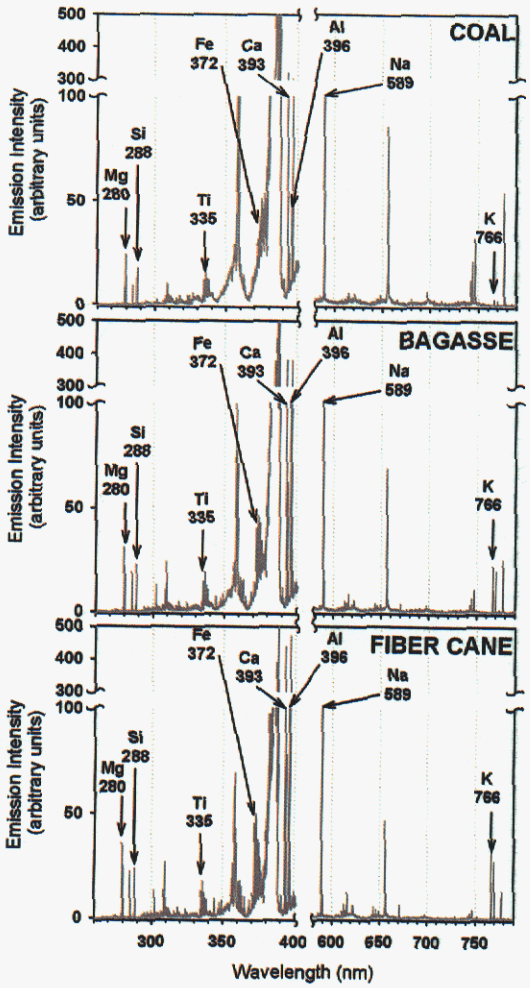

Figure 11. Near-superheater LIBS spectra for Test 1 (coal), Test 2 (bagasse), and Test 3 (fiber cane). Species' peak locations are identified with numbers expressed in nanometers.

In Fig. 11, for clarity, only the spectral region between 260 nm and 790 nm is depicted with the section between 480 nm and 590 nm omitted. The eight elements targeted during data reduction were silicon, aluminum, titanium, iron, calcium, magnesium, sodium, and potassium, and their emission lines are marked by arrows in the figure. Close examination of these spectra (see Appendix A) reveals that, except for iron during Test 1, the lines of interest were well isolated from interferences for quantification. The iron results from Test 1 were discarded. The three spectra in Fig. 11 are qualitatively similar, although the signal levels for the targeted elements vary. The molecule CN is responsible for the relatively broad features near 360 nm and 390 nm.

The peaks near 656 nm, 745 nm, and 780 nm result from H, N, and O emission, respectively. Quantification of H, N, and O concentrations is not straightforward because of their tendency to form molecules such as CN and OH rapidly after plasma initiation.

Post-field-test calibrations were performed in the laboratory using a nebulizer system arranged to deliver a known concentration of each element to the LIBS probe volume.[35] Three-point calibration curves of mass concentration ($\mu g / m^3$ at 300 K and 101 kPa) versus integrated peak area were generated for each element and were used to quantify the signals. The line-center wavelengths used during peak integration are shown in Table 7. For sodium and magnesium, the line-center wavelength was taken as the average of the two line-center wavelengths shown in the table. Integration intervals are also shown in the table. The area under the signal within the integration interval centered symmetrically around the line-center wavelength was calculated. The areas under two baseline regions, each half as wide as the integration interval, were subtracted from the integrated signal. The detailed spectra in Appendix A. provide a visual representation of the signal and baseline intervals. To eliminate complications associated with integrating occasional negative signals generated by the manufacturer-provided spectrometer software, 1000 counts were added to each data point before integration was performed. Because these counts were added to both the "peak" data points and the "baseline" data points, the addition had no net effect on the calculated difference in areas. Integration was performed using the tabular integration function of Interactive Data Language. Linear interpolation was used to calculate function values at the endpoints when the integration limits did not coincide exactly with a pixel wavelength. Calibration spectra are provided in Appendix A.

Table 7 Important information about LIBS data reduction and calibration

Element	Line-center wavelength(s) nm	Integration Interval Width (nm)	Calibration Maximum ($\mu g/m^3$)	Test 1 Average ($\mu g/m^3$)	Test 2 Average ($\mu g/m^3$)	Test 3 Average ($\mu g/m^3$)
Ca	393.37	0.536	1500	1880	*2100	1660
K	766.49	1.37	10400	1970	*27400	*28890
Na	588.99 589.59	2.21	10700	11020	12030	11300
Mg	279.55 280.27	1.23	2700	1080	2480	1660
Si	288.16	0.505	12300	*21160	*37680	*25100
Ti	334.90	0.302	3500	900	900	660
Al	396.15	0.361	10700	12440	*36230	*30700
Fe	371.99	0.220	12700	7400	*34510	*30120

Figure 12 depicts the calibration curves used for the present work. Table 7 depicts the maximum concentration of each element used during calibration and the average concentrations from each of the field tests. The averages marked with asterisks are larger than 130% of the maximum calibration concentrations and required dramatic linear extrapolation of the calibration curves to obtain quantitative results. The validity of linearly extrapolating the calibration curves has not been proven, so absolute concentrations should be interpreted with caution. LIBS calibration

system improvements are ongoing. Concentrations are reported in mass-based parts per million, calculated from the calibrated concentrations (in $\mu g/m^3$, 300K and 101 kPa) using the ideal gas law and assuming the surrounding gas is atmospheric-pressure air at 1200 K.

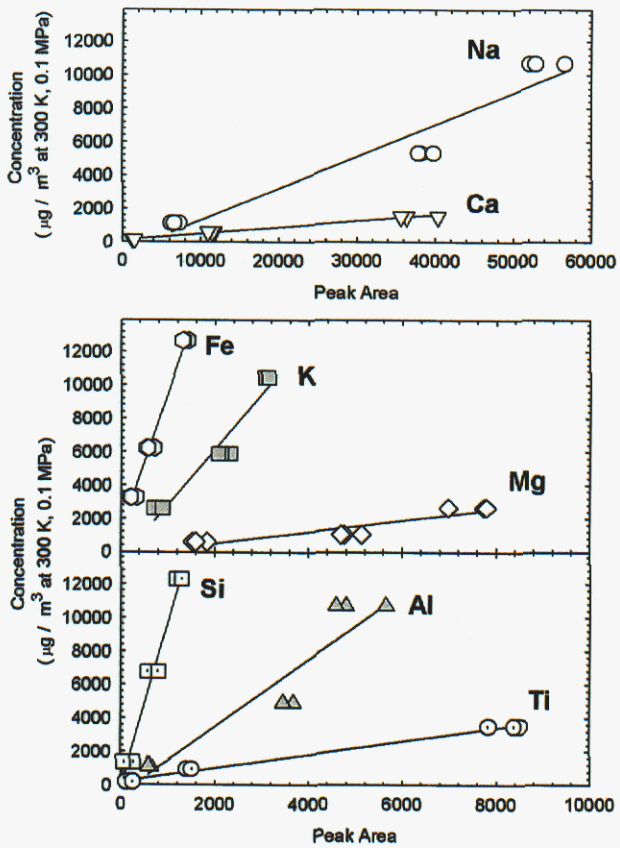

Figure 12. LIBS calibration curves for eight targeted elements.

The LIBS data were collected several hours every day between Jan. 15 and Jan. 24, 2002. Real-time data are presented for Jan. 17 (Test 1, coal) and Jan. 23 (Test 3, fiber cane + bagasse). Data for other days are in Appendix B. Average concentrations and their standard deviations were computed using the intervals shown in Table 8 The intervals were selected as those not affected by spectrometer wavelength calibration drift (see Appendix B for details) or unsteady boiler operation. The LIBS averages account for 12 hours of operation (156 points) during Test 1, four hours (61 points) during Test 2, and 16 hours (231 points) during Test 3.

Table 8 Intervals used for averaging LIBS signals for each fuel.

Test	Fuel	Date	Time Interval	# Hours
1	Coal	January 16	2 p.m. – 6 p.m.	4
1	Coal	January 17	12 p.m. – 6 p.m.	6
1	Coal	January 18	10 a.m. – 11 a.m.	1
2	Bagasse	January 19	10 a.m. -12 p.m.	2
2	Bagasse	January 20	4 p.m. – 6 p.m.	2
1	Coal	January 21	5 p.m. – 7 p.m.	2
3	Fiber Cane	January 23	8 a.m. – 12 p.m.	4
3	Fiber Cane	January 23	1 p.m. – 7 p.m.	6
3	Fiber Cane	January 24	9 a.m. – 12 p.m.	3
3	Fiber Cane	January 24	4 p.m. – 7 p.m.	3

3.3 Results

3.3.1 Stack Gas Concentrations

Figures 13 to 17 depict four-hour traces of exhaust stack O_2, CO_2, CO, NO, and SO_2 concentrations for during each test. At the beginning of the time interval depicted for Test 2, fuel was being switched from coal firing to bagasse co-firing.

Concentrations of all five gases fluctuated more during biomass co-firing (Tests 2-3) than during coal combustion (Test 1). The mean O_2 concentration decreased from 13.3 % for Test 1 to about 12 % for Tests 2 and 3. The mean CO_2 concentration increased from 6.4 % for Test 1 to about 7.7 % for Tests 2 and 3. The higher CO_2 concentration for Tests 2 and 3 are consistent with their higher rates of carbon flow into the boiler depicted in Table 6 (~6400 kg/hr C for Tests 2-3 compared to ~3800 kg/hr C for Test 1). Little can be deduced about the combustion process from these O_2 and CO_2 concentrations because air is known to leak into the boiler. The air leak may be affected by ambient temperature, boiler temperature, pressure fluctuations caused by puffing, and many other variables. Air inleakage is evident from the differences in measured O_2 concentrations at the superheater (e.g., ~9 % for coal) and in the stack (e.g., ~13% for coal).

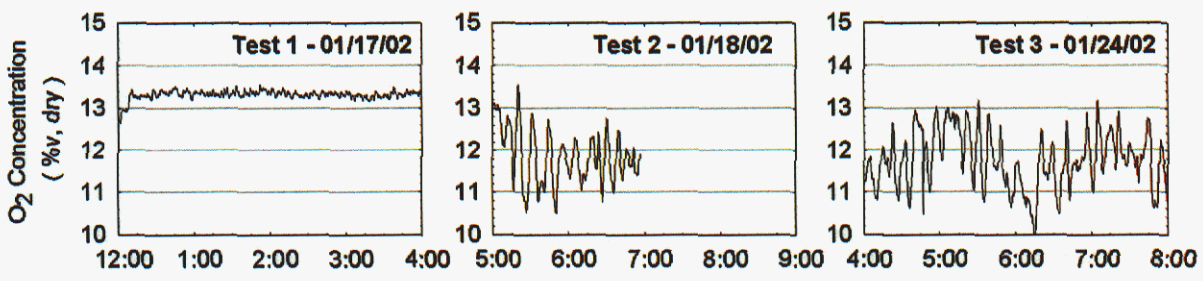

(a) (b) (c)

Figure 13. Sample records of stack O_2 concentration for (a) Test 1, (b) Test 2, and (c) Test 3.

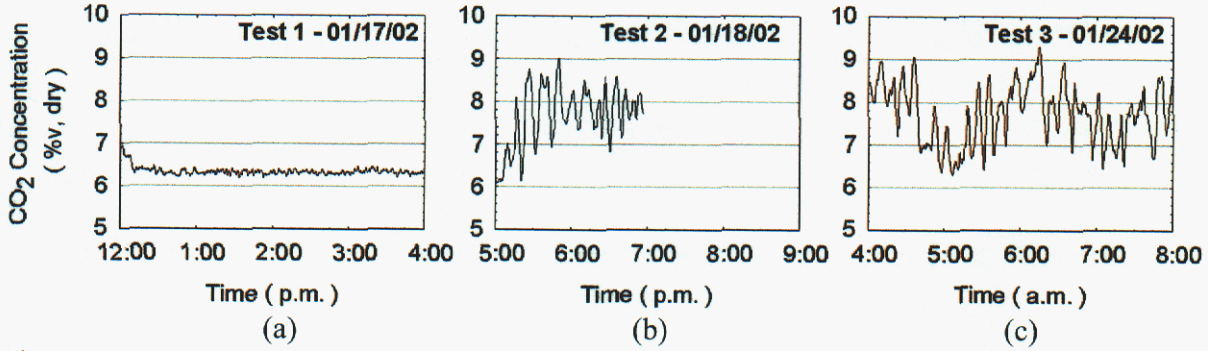

Figure 14. Sample records of stack CO_2 concentration for (a) Test 1, (b) Test 2, and (c) Test 3.

Fig. 15 demonstrates that the mean CO concentrations (normalized to 3 % O_2) were higher for biomass co-firing than for coal. The higher CO concentrations and greater fluctuation levels are consistent with the use of fuels with high moisture concentrations.

Figure 16 shows that normalized NO concentrations were lower for biomass co-firing than for coal combustion in spite of the fact that the rates of fuel nitrogen flow into the boiler (44, 43, and 51 kg/hr for Tests 1, 2, and 3, respectively) do not follow the same trend. The biomass combustion may create less NO because locally rich conditions (Fig. 15) exist where volatiles are released. Additionally, NO can form from N_2 in air. The comparison of these numbers should be made with caution because the rates of air flow into the boiler, either through normal entry ports or through inleakage, are unknown.

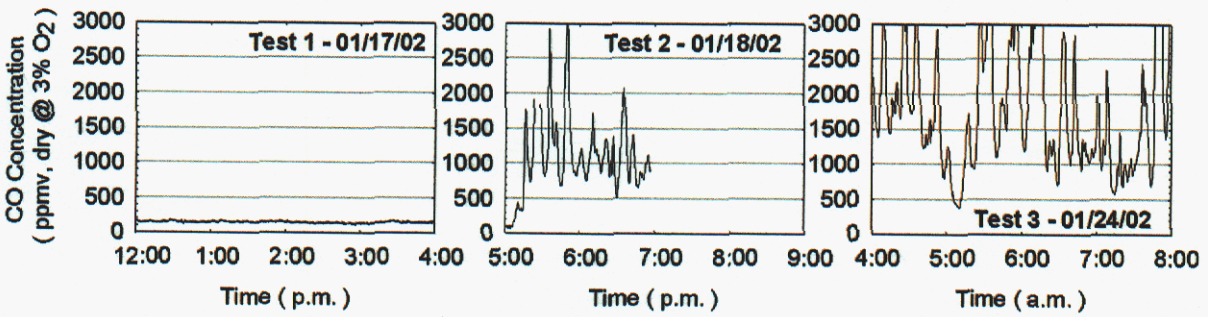

Figure 15. Sample records of stack CO concentration for (a) Test 1, (b) Test 2, and (c) Test 3.

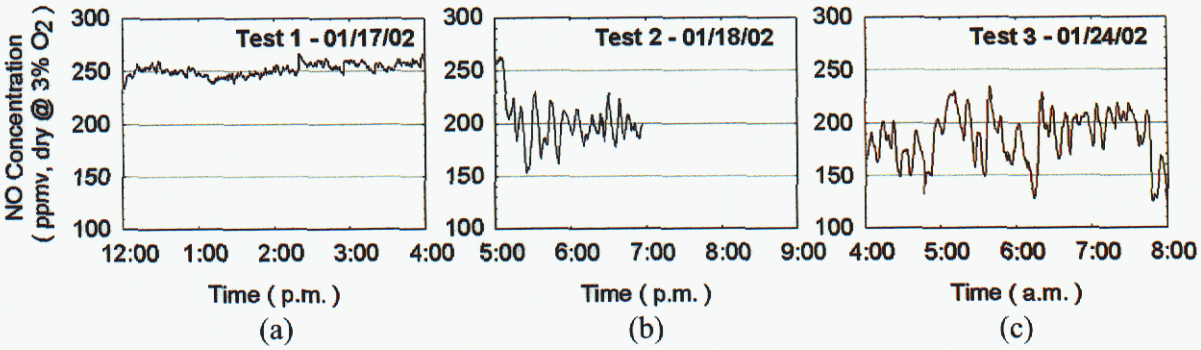

(a) (b) (c)

Figure 16. Sample records of stack NO concentration for (a) Test 1, (b) Test 2, and (c) Test 3.

The SO_2 concentration, shown in Fig. 17, varies irregularly and does not correlate with solid fuel type. The comparison of measured SO_2 concentrations with hourly information from the power plant data historian shown in Fig. 18 reveals that increases and decreases in stack SO_2 concentration sometimes correlate with increases and decreases in Bunker C fuel oil use.

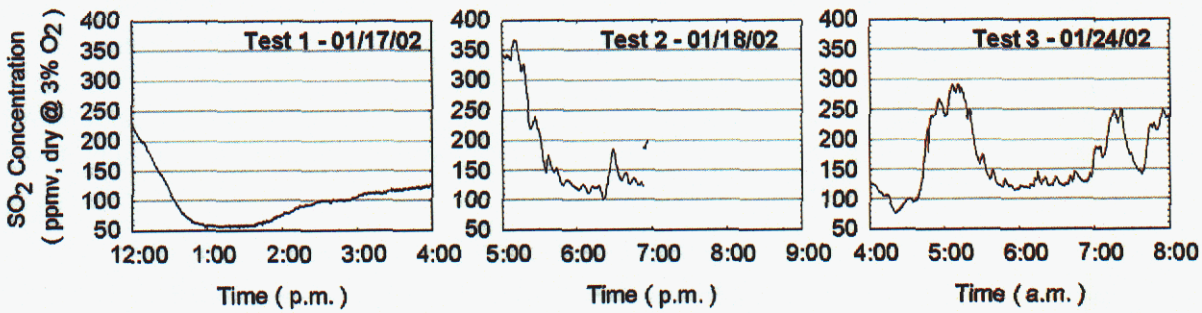

(a) (b) (c)

Figure 17. Sample records of stack SO_2 concentration for (a) Test 1, (b) Test 2, and (c) Test 3.

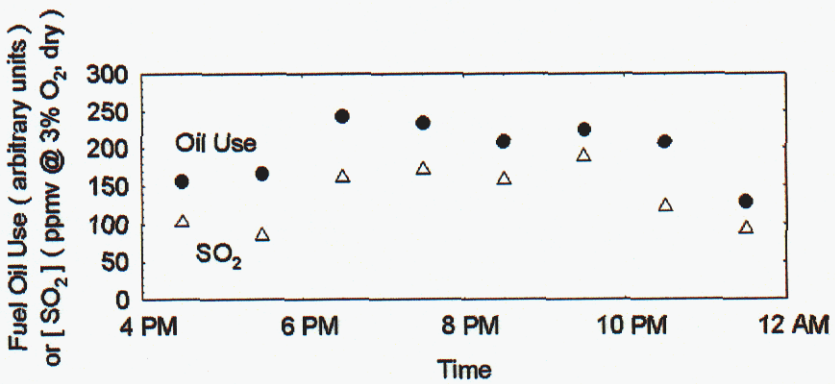

Figure 18. Hourly fuel oil usage from the plant data historian (arbitrary units) along with hourly averages of measured stack SO_2 concentration for eight hours on Jan. 22 (Test 3).

Table 9 compares the Sandia (SNL)-measured stack gas concentrations and those measured during official plant stack testing. Agreement is reasonable. For comparison with laboratory testing, Energy EINOx from the official stack testing are provided. These values were obtained from the official stack testing results (originally provided in lbm/MMBtu). The field Energy EINOx values (0.12–0.18 g/MJ) are within the range of values (0.1–0.3 g/MJ) measured in the laboratory.

Table 9 Comparison of average Sandia-measured exhaust concentrations with those measured during stack gas testing. Averages are for four-hour traces in Figs. 13-17.

Gas	Test 1		Test 2		Test 3	
	SNL	Stack	SNL	Stack	SNL	Stack
O_2, %v dry	13.3	13.9	11.9	12.1	11.8	12.3
CO_2, %v dry	6.3	6.4	7.6	8.4	7.7	7.9
CO, ppmv dry @ 3 % O_2	150	264	1053	1800	1881	1168
NO, ppmv dry @ 3 % O_2	252	319	201	228	186	248
SO_2, ppmv dry @ 3 % O_2	99	287	181	124	165	196
Energy EINOx, g/MJ		0.181		0.116		0.131

3.3.2 Near-Superheater Gas Velocity

Figure 19 shows pitot tube differential pressure for the dominant flow direction at 0.3 m from the inner surface of the boiler wall for Test 1 and Test 3. As with the major gas concentrations, the level of data fluctuation for biomass co-firing was higher than that for coal combustion. As can be seen in the figure, the differential pressures occasionally exceeded the maximum measurable differential pressure (0.93 mm Hg or 0.5 inches of water) during biomass co-firing. Average velocities for the biomass cases may thus be biased toward lower velocities.

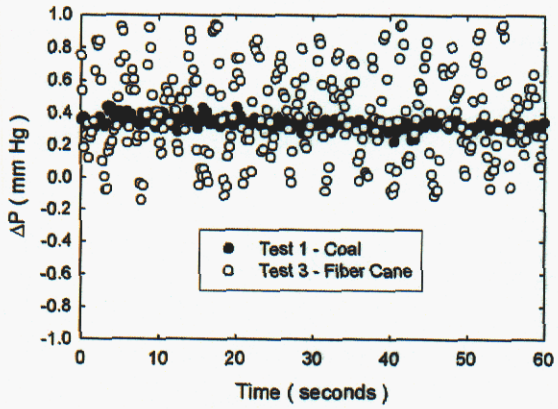

Figure 19. One minute of pitot tube differential pressure measurements for the dominant flow direction 0.3 m from the wall the during Tests 1 and 3.

Figure 20 shows profiles of the average and standard deviation of velocity in the dominant flow direction for all tests. For Tests 1 and 2, velocity increases, levels off, and then decreases as distance from the wall increases. This behavior may indicate the presence of large scale flow structures. Test 3 velocities increase or remain constant with distance. The LIBS-measurement-location (0.6 m from the wall) velocity is about 16 m/s for each test. A jet-in-crossflow analysis revealed that the effect of the 18 L/min nitrogen purge flow on the concentrations at the location of the LIBS spark was minimal. The influence of the purge on measured concentration was found to be significant only for crossflow velocities below about 1.5 m/s.

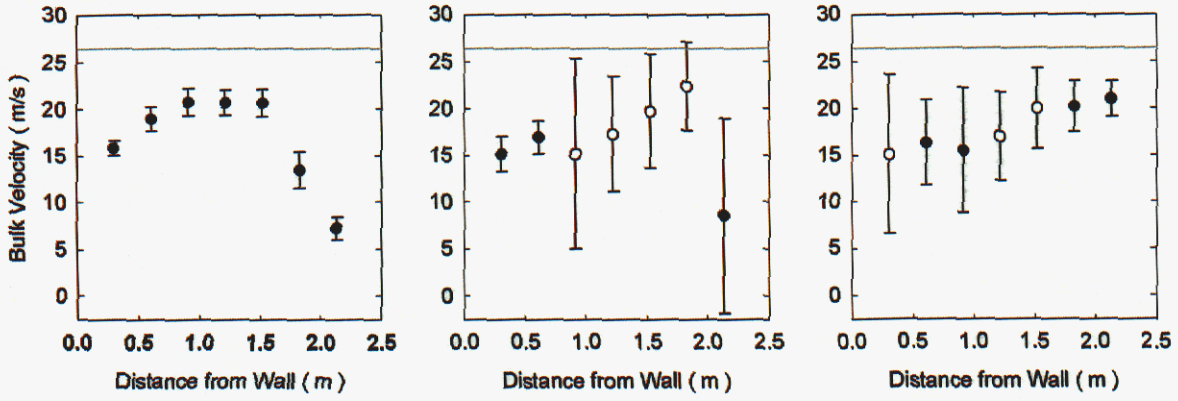

(a) (b) (c)

Figure 20. Average velocity for (a) Test 1, (b) Test 2, and (c) Test 3 . Open symbols show data for which differential pressure exceeded maximum measurable value (horizontal lines).

3.3.3 Near-Superheater Particle Loading

Typical SEM images with two levels of magnification of particles are shown in Fig. 21. The coal-produced particles are relatively uniform in size with a maximum size of about 3 μm. In contrast, the size distributions for the biomass co-firing cases appear more broad, with agglomerates and particles as large as 5 μm to 10 μm appearing. Co-firing of biomass appears to produce more ultrafine particles (less than 1 μm in size) than coal, in agreement with previous findings.[27] Particles a few microns in size can be vaporized using LIBS.[36]

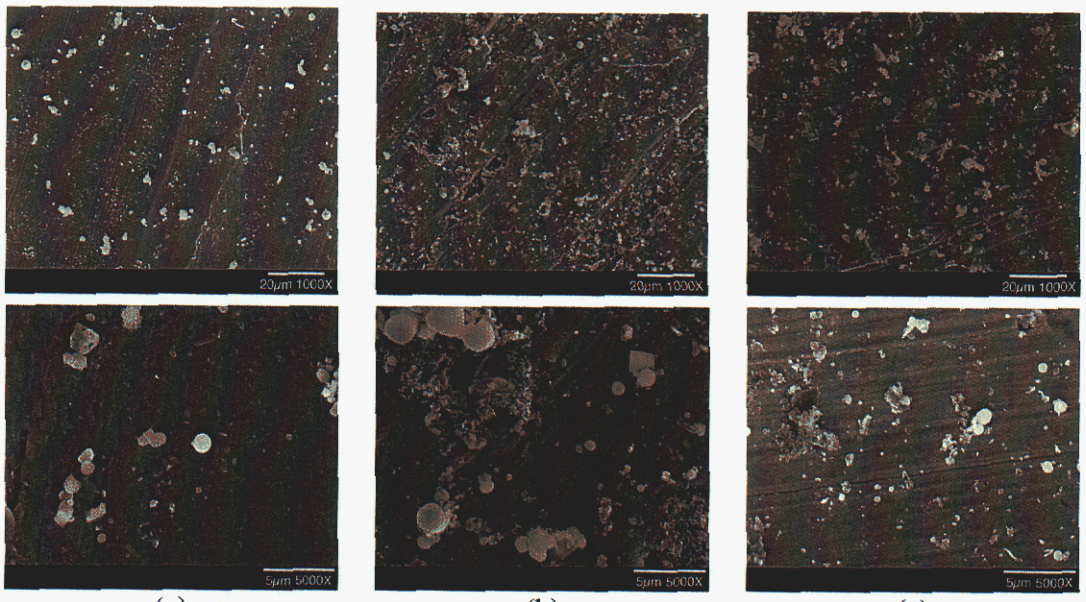

(a) (b) (c)

Figure 21. SEM images of particles collected during (a) Test 1, (b) Test 2, and (c) Test 3.

3.3.4 Near-Superheater Inorganic Concentrations

Figures 22(a) and 22(b) show daily LIBs-measured concentration traces for Test 1 and Test 3, respectively. The figures demonstrate typical concentrations and their variations with time. The ordinate range of the bottom panels is 10% of those of the other panels. Concentration fluctuation levels are higher for the biomass co-firing test, consistent with the gas concentration and velocity measurements reported above and with fluctuations known to occur during combustion of wet biomass fuel.[8] The concentrations of silicon, titanium, calcium, magnesium, and sodium are similar for the two tests. The concentrations of aluminum and potassium are higher for the fiber cane test than for the coal test. At about 4 p.m. on January 23, because of irregularities in loading the bagasse house, it was observed that fiber cane began feeding into the boiler at a rate greater than the average rate shown in Table 4. Resulting increases in aluminum, iron, and potassium concentrations are noticeable in Fig. 22(b). The exact rate of fiber cane flow could not be determined, but the LIBS signals confirmed the feed rate enhancement. The data in Fig. 22 show that LIBS can track fuel or boiler chemistry changes in real time. An information-rich and continuous stream of data can be obtained using LIBS in the field, which has advantages over collecting physical fuel samples at discrete time intervals and waiting days or weeks for results from traditional analyses.

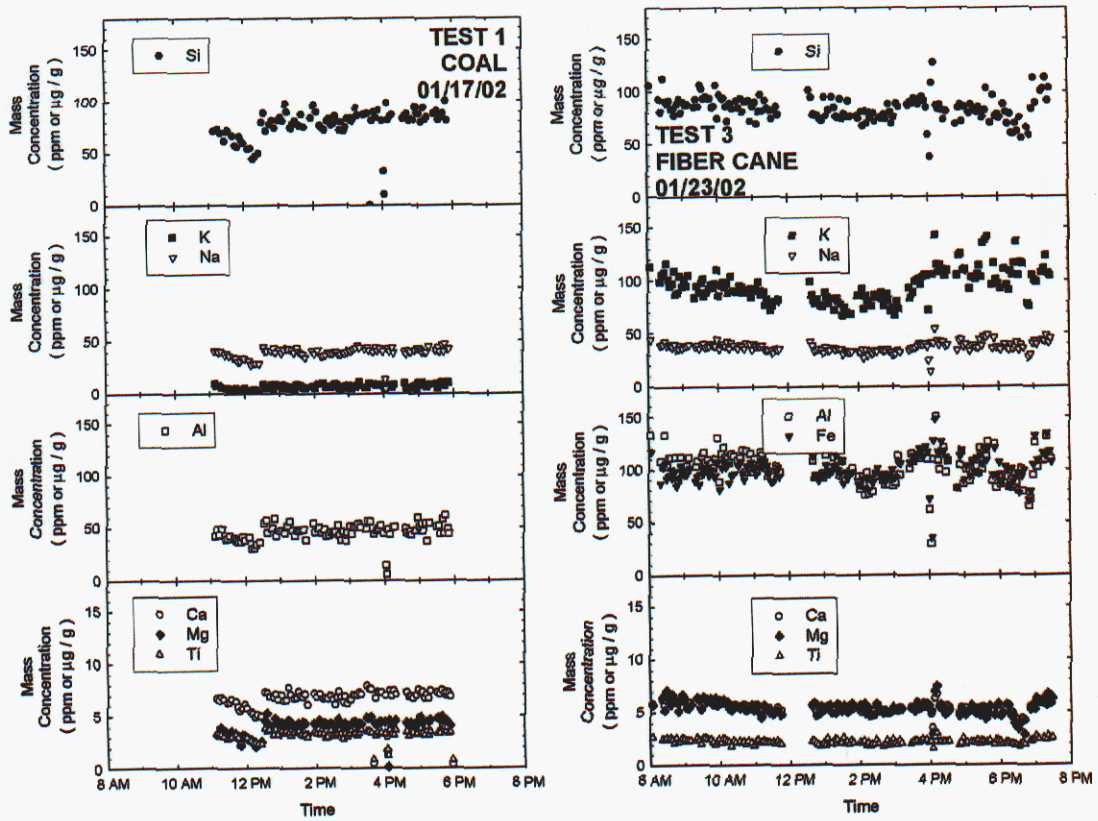

Figure 22. LIBS-measured concentrations during Test 1 and Test 3.

Figure 23 shows the average LIBS-measured concentration of each element for the three tests. The vertical bars show standard deviations. For coal combustion, silicon and aluminum are the major components, consistent with the usual prevalence of aluminosilicates in bituminous coal ash. Tests 2 and 3, the two biomass co-firing cases, exhibit similar chemical distributions at the measurement location. The major biomass-formed constituents are also silicon and aluminum, but iron and potassium also play major roles. All of the fuels exhibit similar concentrations of titanium, calcium, magnesium, and sodium. The LIBS measurement may be biased toward fume-forming components such as alkali metals, alkaline earth metals and even iron; this is because refractory fly ash components such as silicon, aluminum, and titanium may not be completely vaporized in the LIBS spark and thus may be underestimated.

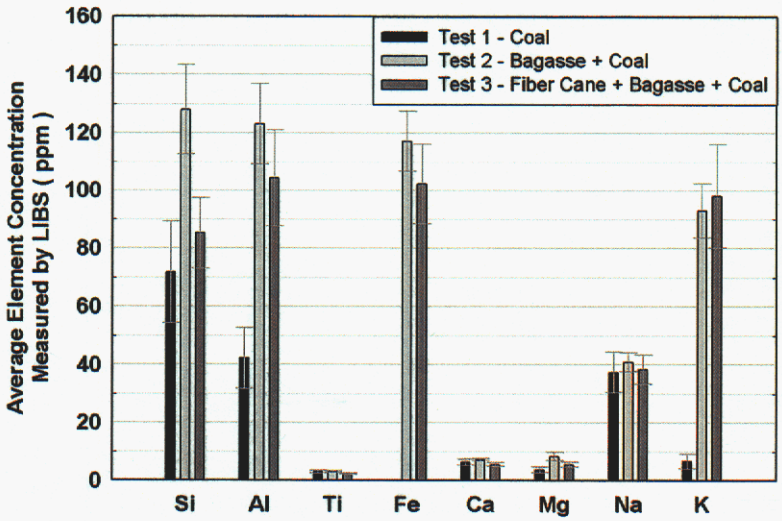

Figure 23. Average element mass concentrations measured by LIBS. The vertical bars represent standard deviations in the LIBS measurements.

Figure 24 shows the rate of flow of each element into the boiler estimated using fuel flow rate, proximate analysis, and ash chemistry. A complete mass balance would consider the rate of bottom ash loss, but this was not measured. Additionally, using fuel ash analyses to estimate inorganic concentrations in the fuel may underestimate these quantities because atomically dispersed elements are undercounted using standard ash analyses.[37] For coal combustion, silicon and aluminum are predicted to be the major inorganics. The LIBS results agree. The predicted chemical compositions for the two biomass co-firing cases are similar; the similarity between the two biomass blends is also captured by the LIBS measurements. Silicon, aluminum, and iron are predicted to be the major constituents of the co-firing combustion products. The LIBS measurements reflect this trend too, although potassium is measured to also play an important role. The fuel-chemistry predictions do not support the important role that sodium is measured to play for all fuels using LIBS. Hence, the combustion products are measured to be enriched relative to the parent fuels in potassium for the biomass tests and in sodium for all three tests.

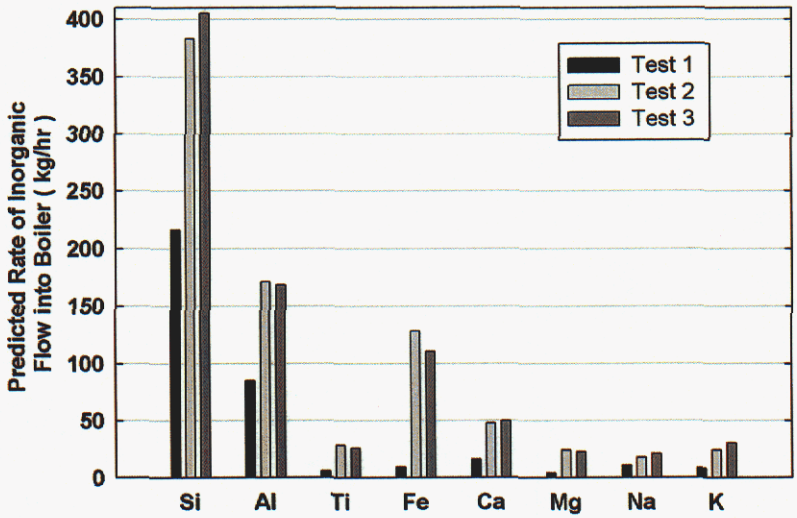

Figure 24. Predicted rates of element flows into the boiler.

The LIBS-measured enrichment in potassium for biomass and sodium for all three fuels can be further analyzed by comparison to fuel ash and bottom ash chemistry. Figure 25 shows element concentrations—expressed as mass percentages for the eight elements of interest—for the fuel ash and the bottom ash from each test. If the concentration of a given element is higher in the fuel ash than in the bottom ash, the element can be expected to be enriched in the combustion products. The figure shows that the Test 1 fuel ash and bottom ash are virtually identical, suggesting that the bottom ash inorganics are derived from coal ash. It follows that the inorganics released into the boiler will similarly come from coal ash. This suggests that the eight elements should not be enriched in the Test 1 combustion products relative to the fuel. Sodium, a minor component of the fuel ash, is observed to be enriched for Test 1. For Tests 2-3, the fuel ash has higher concentrations of iron and potassium than the bottom ash. An enrichment in iron is difficult to distinguish in the LIBS measurements, but the enrichment in potassium is apparent. The fuel and bottom ash chemical compositions do not explain the LIBS-observed sodium enrichment results. This may be because of the aforementioned uncertainty in fuel ash analysis for atomically dispersed elements, such as potassium, sodium, magnesium, and calcium.

Compounds containing sodium and potassium and to a lesser extent calcium and magnesium are more readily volatilized into the combustion space than those in more refractory or mineral forms such as silicon, aluminum, and titanium. The alkali metals and even iron are likely to form fume particles during and after combustion, while the true minerals should form larger fly ash particles. Bituminous coal is expected to contain inorganics in mostly mineral forms, while biomass is expected to be more populated by atomically dispersed or ionic forms of some species.[37] The apparent enrichment in sodium concentration for all fuels and in potassium concentration for the biomass fuels may be caused by atomically dispersed alkali metals not measurable using ash analyses. To minimize bias in ash measurement toward refractory metals, future tests should be performed using low-temperature ash evaluation.

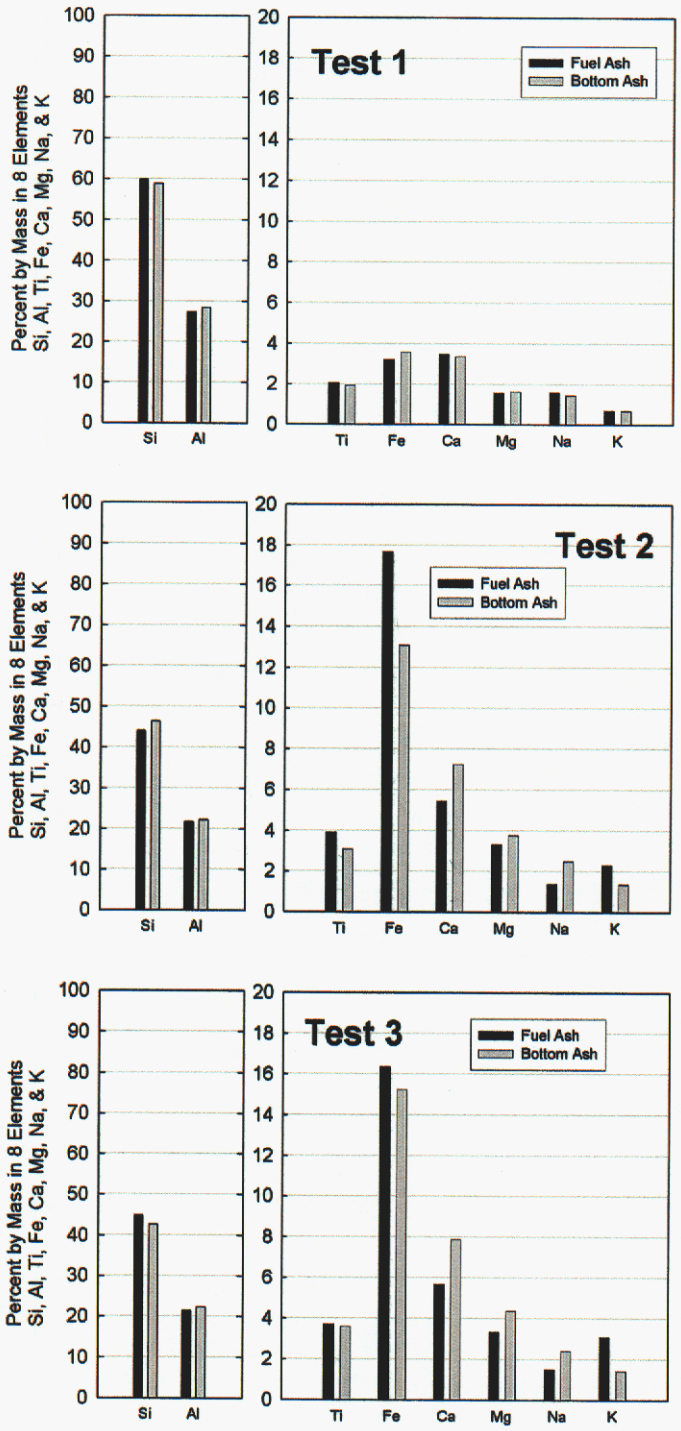

Figure 25. Mass concentrations of eight targeted elements in the fuel ash and bottom ash for each of the three tests.

Figure 26 compares the LIBS-determined combustion product concentrations with the mock superheater tube deposit compositions determined from ash analyses. Sodium (for all tests) and potassium (for the biomass tests) have higher concentrations in the flowing combustion products than in the deposit. This is consistent with the presence of volatilized alkali metals in a vapor or a fume with deposition dominated by inertial impaction and eddy impaction of larger ash particles. Iron also appears to have higher concentrations in the flowing combustion products than in the deposit; iron is known to form a fume under certain conditions during coal combustion, so this is also consistent with impaction as the dominant mechanism of ash deposition at this location.

3.3.5 Comments on LIBS

The present work represents the first application of LIBS in the high-temperature region of a boiler.[34] Many challenges were overcome successfully, including the design and deployment of a cooled and purged optics probe. The concentrations of eight elements were detected simultaneously for the first time using a relatively new and powerful detector, the echelle spectrometer. Lessons were learned about the operation and maintenance of this instrument in a harsh field environment. The present LIBS measurements and results do raise some important questions about the technique that should be resolved in future research. Several LIBS issues are delineated here:

- The smallest particles and gases will be fully detectable by LIBS. However, larger fly ash particles may not be fully vaporized in the LIBS spark. Hence, the relative concentrations of elements such as silicon, aluminum, and titanium may be underestimated by the LIBS measurements. As a result, relative concentrations of calcium, magnesium, sodium, potassium, and/or iron may be overestimated using LIBS. Determining the range of sizes of boiler particles fully vaporizable by LIBS is a good future research topic.
- Another important consideration is that the LIBS measurement is made close to the boiler wall, although species and temperature gradients undoubtedly exist in the boiler. Determining whether or not the point measurement is representative of the entire cross section is another excellent future research topic.
- The current Sandia LIBS calibration rig was developed for lower concentrations than those that appeared in the biomass boiler. While the existence of large signals is desirable and shows the potential of LIBS for this type of application, the applicability of the linear calibrations for large concentrations in the present report is unclear. Development of a calibration rig applicable for the current conditions is a goal of future Sandia LIBS work.
- It was assumed that the LIBS instrument responds to elements in the field the same way it responds to the laboratory aerosol. Experiments were not performed to verify this assumption. Examination of the effects of field conditions such as high temperature and high particle loading on calibration is an important future research topic.
- More detailed analyses to determine minimum detection limits and shot-to-shot variations in the LIBS signals should be pursued in future efforts.

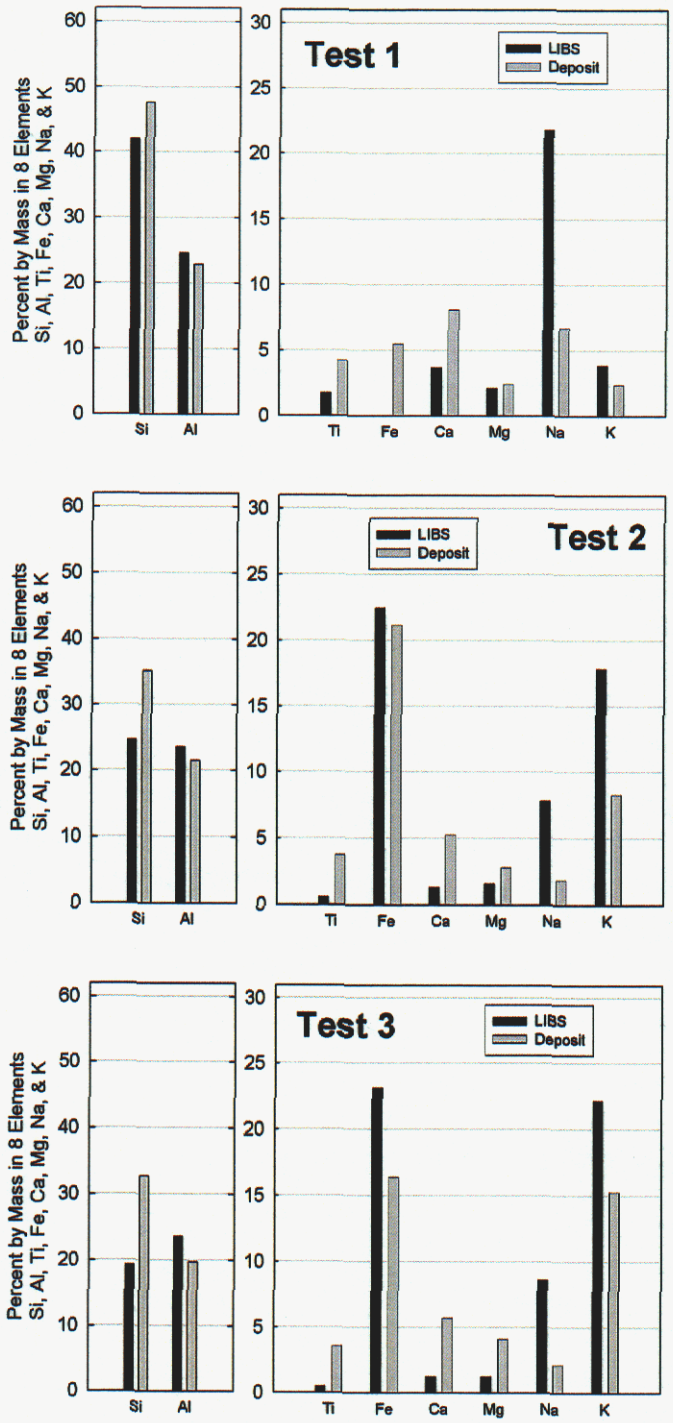

Figure 26. Mass concentration of each element expressed as a percentage of the total amount of the eight targeted elements for LIBS and for the mock superheater deposit.

3.4 Summary and Conclusions of Field Tests

Measurements were made of stack gas concentrations, near-superheater velocities, near-superheater particle loading, and near-superheater inorganic concentrations during coal combustion and biomass co-firing in a full-scale boiler. The techniques employed were conventional stack gas analysis, pitot tube probing, impaction coupon collection, and laser-induced breakdown spectroscopy. The levels of fluctuation of stack gas concentrations, velocities, and inorganic concentrations were higher for biomass co-firing than for coal combustion. Stack O_2 and CO_2 concentrations were lower and higher, respectively, for biomass co-firing than for coal combustion. Mean normalized CO and NO concentrations were higher and lower, respectively, for biomass co-firing than for coal combustion. Stack SO_2 concentration correlated with Bunker C fuel oil use and did not reflect changes in solid fuel use. Velocity measurements revealed a spatially non-uniform velocity distribution across the duct. The LIBS measurement location velocity was about 16 m/s for all fuels. Qualitatively, particles at the LIBS measurement location originating from coal combustion had a more narrow size distribution than those from biomass co-firing. The biomass tests appeared to produce more fine particles. LIBS produced an information-rich and continuous stream of data consisting of strong signals from silicon, aluminum, titanium, iron, magnesium, calcium, sodium, and potassium. Changes in fuel makeup were successfully detected. The major inorganic constituents of the fuel ash were also the major measured constituents in the combustion products. The combustion products were enriched in sodium relative to the fuel ash during all tests. For biomass co-firing, the boiler flow was enriched in potassium relative to the fuel ash. The sodium and potassium enrichments indicate that the alkali metals exist in dispersed forms more readily releasable into the combustion products than refractory components such as silicon, aluminum, and titanium. Relative to the measured deposit chemistry, the combustion flows were enriched in iron, sodium, and potassium, constituents that are known to form fumes. This indicates that particle impaction is the dominant deposition mechanism at the superheater and that fume material deposition is less important.

4 Overall Summary and Conclusions

Laboratory (pilot) scale testing and full scale testing were performed to assess the effects of co-firing fiber cane with coal. The laboratory tests revealed that, because biomass fuels convert their nitrogen to NO more readily than coal under entrained flow conditions, fiber cane/coal co-firing produced the same amount of NO per unit energy input as coal combustion. In the full-scale boiler, biomass co-firing produced less NO per unit energy input than coal combustion. Several differences between the laboratory and boiler tests were delineated; key differences included higher temperatures, better mixing, higher heating rates, smaller fuel particle sizes, different oxygen concentrations, and lower moisture in the MFC than in the boiler.

LIBS showed that the combustion products at the superheater were enriched in sodium for all tests and potassium for the biomass co-firing tests relative to the fuel ash. Compared to mock superheater deposits collected during testing, the combustion products were enriched in sodium, potassium, and iron. The enrichment in the alkali metals and in iron is consistent with the formation of fumes containing these constituents in the boiler. Ash deposition appeared to be dominated by impaction at the superheater.

5 Acknowledgments

This project was co-funded by the U.S. DOE (Cooperative Agreement DE-FC36-99G010479), HC&S, and the Hawaii Natural Energy Institute. The DOE BioPower Program under the direction of Raymond Costello supported Sandia's involvement. Many thanks go to James Spaeth of the DOE for his guidance. Ralph Overend and Wade Amos of the National Renewable Energy Laboratory are acknowledged for their advice and attention in the field. Several Sandians contributed to the success of this project; they are Larry Baxter, Ben Wu, Doug Scott, Howard Johnsen, Gian Sclippa, Gilbert Hofacker, Sal Birtola, Shane Sickafoose, Nancy Yang, Clay Horiuchi, Alejandro Molina, and Chris Shaddix. Finally, the HC&S boiler operators and staff are graciously thanked for their hard work and patience. Sandia is a multiprogram laboratory operated by Sandia Corporation, a Lockheed Martin Company, for the United States Department of Energy's National Nuclear Security Administration under Contract DE-AC04-94AL85000.

6 References

1. Lamb, B.W. and Bilger, R.W., "Combustion of Bagasse: Literature-Review," *Sugar Technology Reviews*, 4:89-130 (1977).
2. Mcburney, B. and Mcburney, J.C., "Designing Bagasse Fired Boilers for Low Emissions 2," *International Sugar Journal*, 99:133(1997).
3. Mcburney, B. and Mcburney, J.C., "Designing Bagasse Fired Boilers for Low Emissions 1," *International Sugar Journal*, 99:58-64 (1997).
4. Dixon, T.F., "Steam Generation and Combustion Research at the SRI," *International Sugar Journal*, 101:219-220 (1999).
5. Soler, P.B., Sauvanell, A.L.B., Hernandez, A.A., and Safon, R.B., "Modifications for Suspension Burning of Bagasse," *International Sugar Journal*, 101:520-522 (1999).
6. Cruz, I., Feria, J., Arrascaeta, A., and Friedman, P., "Boiler Remodeling for the Combustion of Dried Bagasse," *International Sugar Journal*, 93:75-78 (1991).
7. Rasul, M.G. and Rudolph, V., "Fluidized Bed Combustion of Australian Bagasse," *Fuel*, 79:123-130 (2000).
8. Woodfield, P.L., Kent, J.H., and Dixon, T.F., "Computational Modelling of Combustion Instability in Bagasse-Fired Furnaces," *Experimental Thermal and Fluid Science*, 21:17-25 (2000).
9. Luo, M. and Stanmore, B.R., "Modeling Combustion in a Bagasse-Fired Furnace .1. Formulation and Testing of the Model," *Journal of the Institute of Energy*, 67:128-135

(1994).
10. Harel, P. and Baguant, J., "Bagasse Combustion," *International Sugar Journal*, 94:11-20 (1992).
11. Nassar, M.M., Ashour, E.A., and Wahid, S.S., "Thermal Characteristics of Bagasse," *Journal of Applied Polymer Science*, 61:885-890 (1996).
12. Drummond, A.R.F. and Drummond, I.W., "Pyrolysis of Sugar Cane Bagasse in a Wire-Mesh Reactor," *Industrial & Engineering Chemistry Research*, 35:1263-1268 (1996).
13. Stubington, J.F. and Aiman, S., "Pyrolysis Kinetics of Bagasse at High Heating Rates," *Energy & Fuels*, 8:194-203 (1994).
14. Aiman, S. and Stubington, J.F., "The Pyrolysis Kinetics of Bagasse at Low Heating Rates," *Biomass & Bioenergy*, 5:113-120 (1993).
15. Luo, M.C. and Stanmore, B., "The Combustion Characteristics of Char From Pulverized Bagasse," *Fuel*, 71:1074-1076 (1992).
16. Varhegyi, G., Antal, M.J., Szekely, T., and Szabo, P., "Kinetics of the Thermal-Decomposition of Cellulose ; Hemicellulose ; and Sugar-Cane Bagasse," *Energy & Fuels*, 3:329-335 (1989).
17. Ouensanga, A. and Picard, C., "Thermal-Degradation of Sugar-Cane Bagasse," *Thermochimica Acta*, 125 :89-97 (1988).
18. Varhegyi, G., Antal, M.J., Szekely, T., Till, F., Jakab, E., and Szabo, P., "Simultaneous Thermogravimetric Mass-Spectrometric Studies of the Thermal-Decomposition of Bio-Polymers .2. Sugar-Cane Bagasse in the Presence and Absence of Catalysts," *Energy & Fuels*, 2:273-277 (1988).
19. Rasul, M.G., Rudolph, V., and Carsky, M., "Physical Properties of Bagasse," *Fuel*, 78:905-910 (1999).
20. Nebra, S.A. and Macedo, I.D., "Bagasse Particles Shape and Size and Their Free-Settling Velocity," *International Sugar Journal*, 90:168-170 (1988).
21. Ponce, N., Friedman, P., and Leal, D., "Geometric-Properties and Density of Bagasse Particles," *International Sugar Journal*, 85:291-295 (1983).
22. Stubington, J.F. and Fenton, H., "Combustion Characteristics of Dried and Pelletized Bagasse," *Combustion Science and Technology*, 37:285-299 (1984).
23. Cundy, V.A., Maples, D., and Tauzin, C., "Combustion of Bagasse: Use of an Agricultural-Derived Waste," *Fuel*, 62:775-780 (1983).
24. Lora, E.S. and Gomez, O., "Bagasse Suspension Burning and Air-Pollution," *International Sugar Journal*, 97:683-&(1995).
25. Farabi, H. and Ramroop, I., "Bagasse: Controlling Pollution From a Free Fuel," *International Sugar Journal*, 96:221-224 (1994).
26. Turn, S., Kinoshita, C., Jakeway, L., Jenkins, B., Baxter, L., Wu, B., and Blevins, L., "Fuel characteristics of processed, high-fiber sugarcane," *Fuel Processing Technology*,81:35-55 (2003).
27. Blevins, L. G. and Cauley, T. H.,. "Fine Particulate Formation during Switchgrass/Coal Cofiring," *ASME Journal of Engineering for Gas Turbines and Power,* In Press (2004).
28. Baxter, L.L., "Char Fragmentation and Fly-Ash Formation During Pulverized-Coal Combustion," *Combustion and Flame*, 90:174-184 (1992).

29. Baxter, L.L., Hencken, K.R., and Harding, N.S., "The Dynamic Variation of Particle Capture Efficiency During Ash Deposition in Coal-Fired Combustors," *Proceedings of the Combustion Institute*, 23:993-999 (1990).
30. Molina, A., Eddings, E.G., Pershing, D.W., and Sarofim, A.F., "Char Nitrogen Conversion: Implications to Emissions From Coal-Fired Utility Boilers," *Progress in Energy and Combustion Science*, 26:507-531 (2000).
31. Smoot, L.D., "Coal and Char Combustion," Fossil Fuel Combustion: A Source Book, pp. 653-781, John WIley and Sons, Inc. (1991).
32. Anonymous, "Emission Testing at Hawaiian Commercial & Sugar Company Puunene Mill Boiler 1 Stack," Prepared by TetraTech EM Inc., Bakersfield, CA, under contract to Sierra Research, Sacramento, CA (2002).
33. Anonymous, "Series 160S "S" Type Pitot Tubes Operating Instructions - Flow Curves," Dwyer Bulletin H-12, Dwyer Instruments, Inc., Michigan City, Indiana (1997).
34. Blevins, L.G., Shaddix, C.R., Sickafoose, S.M., and Walsh, P.M. , "Laser-Induced Breakdown Spectroscopy in High-Temperature Industrial Boilers and Furnaces," *Applied Optics*, 42:6107-6118 (2003).
35. Hahn, D.W., Carranza, J.E., Arsenault, G.R., Johnsen, H.A., and Hencken, K.R., "Aerosol Generation System for Development and Calibration of Laser-Induced Breakdown Spectroscopy Instrumentation," *Rev Sci Instrum*, 72:3706-3713 (2001).
36. Hahn, D.W. and Lunden, M.M., "Detection and Analysis of Aerosol Particles by Laser-Induced Breakdown Spectroscopy," *Aerosol Science and Technology*, 33:30-48 (2000).
37. Baxter, L.L., "Ash Deposition During Biomass and Coal Combustion : a Mechanistic Approach," *Biomass & Bioenergy*, 4: 85-102 (1993).

APPENDIX A

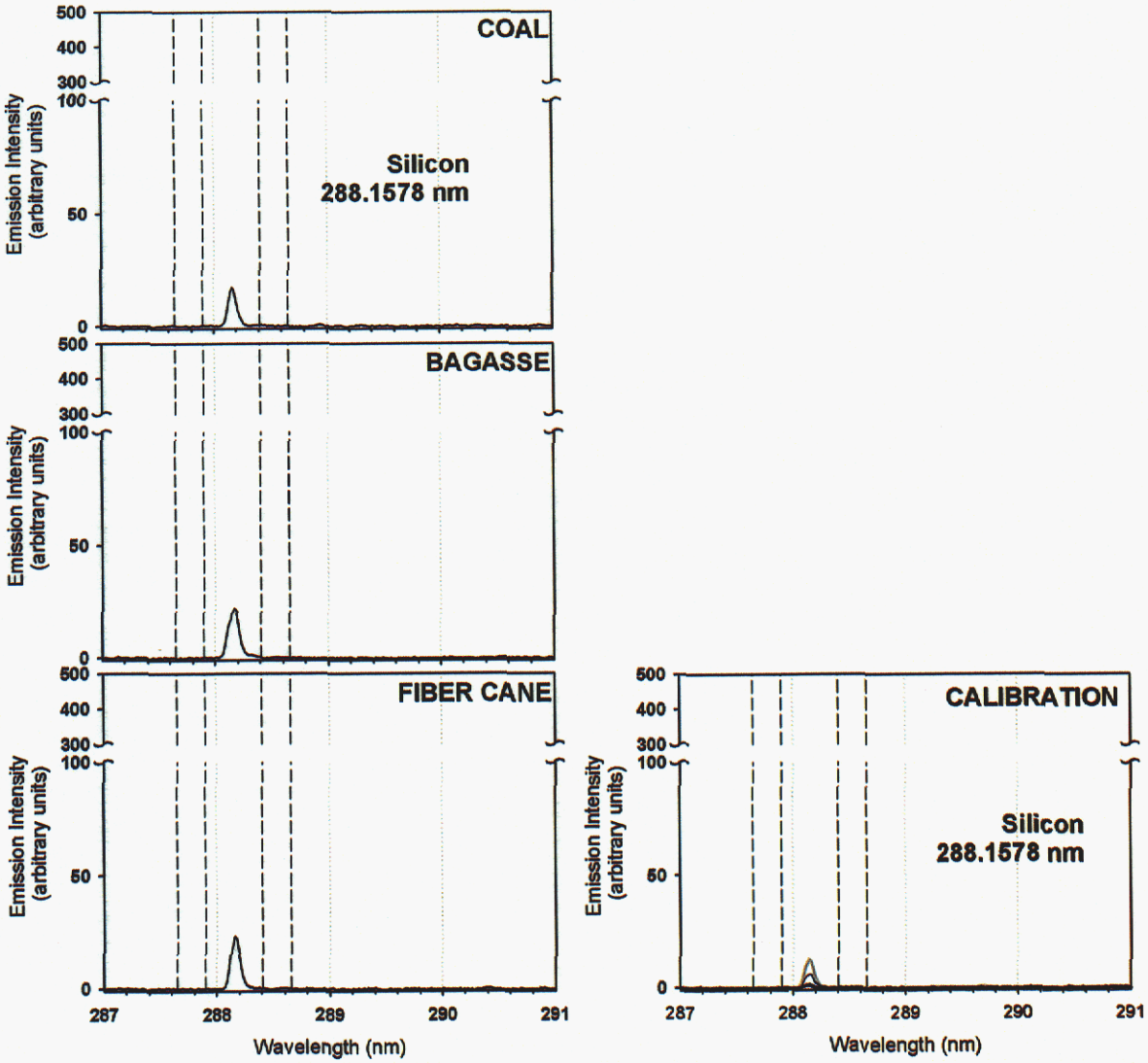

Figure A.1. Silicon signals for the three spectra in Fig. 11 and the calibration spectra. Dashed lines show integration limits for peak area (region between inner dashed lines) and baseline area (leftmost and rightmost regions formed by outer dashed lines and inner dashed lines). The width of the peak area is equal to the combined width of the baseline regions. Baseline area is subtracted from peak area before constructing calibration curves or quantifying signals.

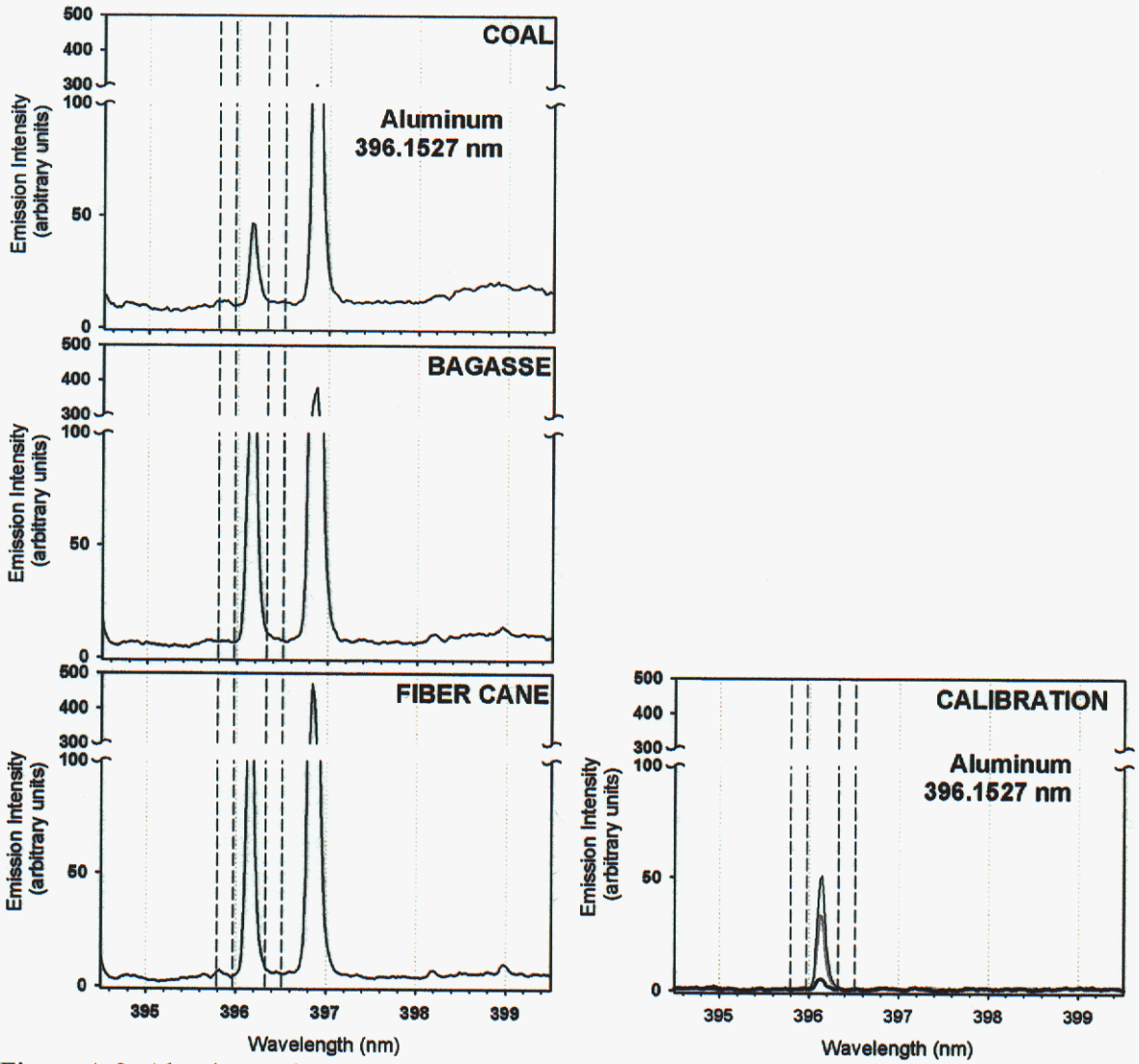

Figure A.2. Aluminum signals for the three spectra in Fig. 11 and the three calibration spectra.

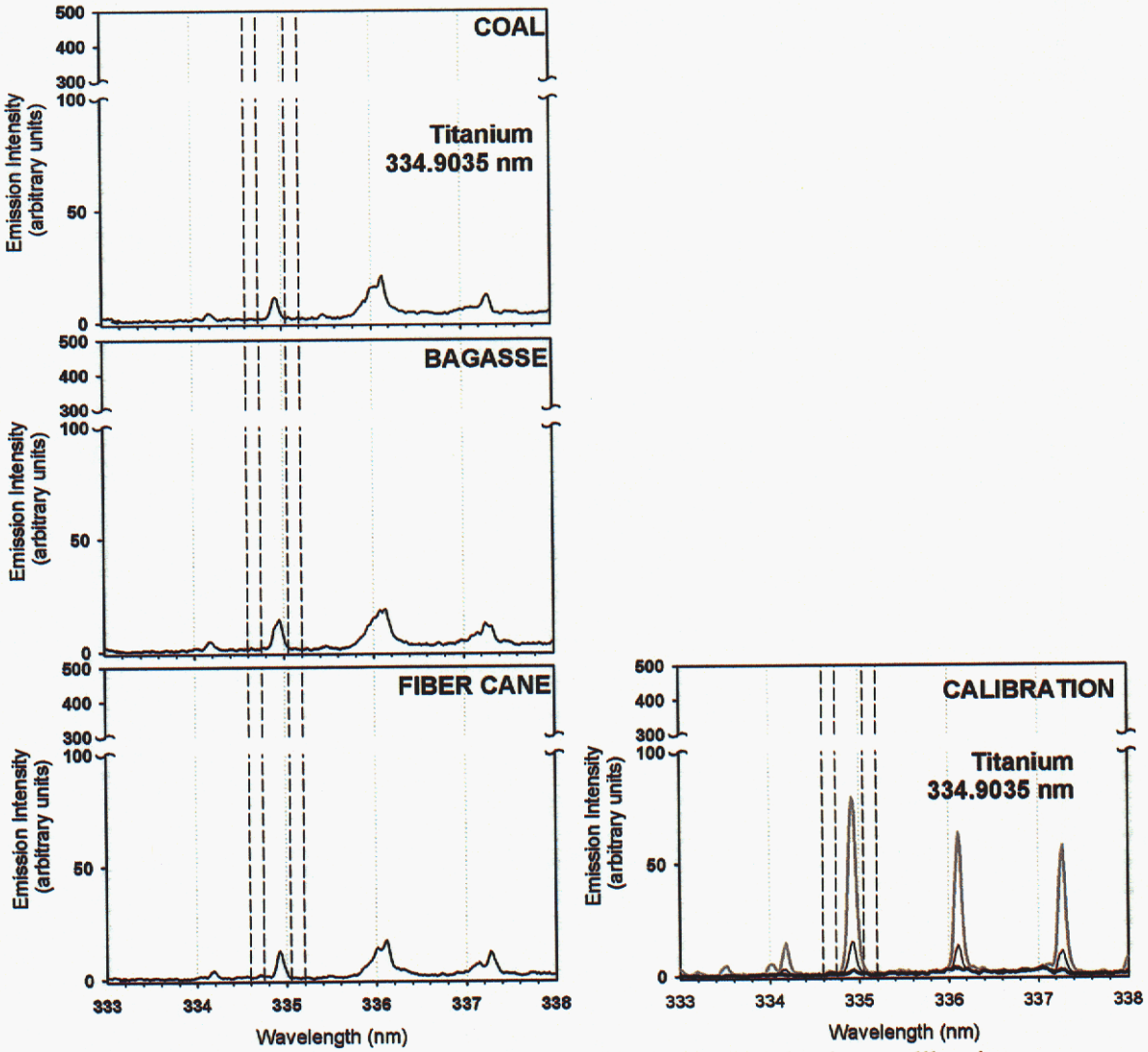

Figure A.3. Titanium signals for the three spectra in Fig. 11 and the three calibration spectra.

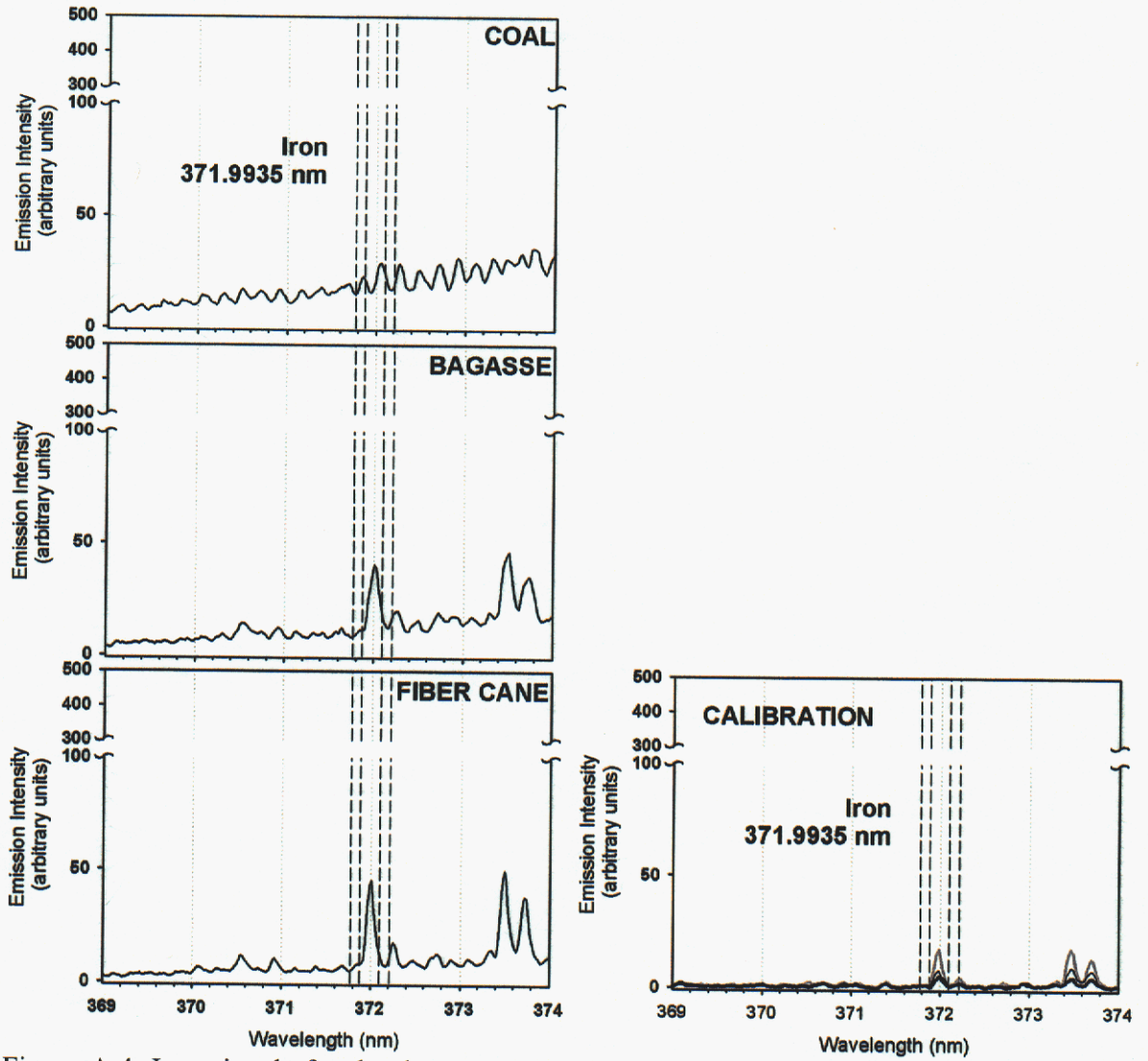

Figure A.4. Iron signals for the three spectra in Fig. 11 and the three calibration spectra. The field tests show a baseline interference in the iron signal. The iron data for coal cannot be distinguished from the baseline and thus were discarded.

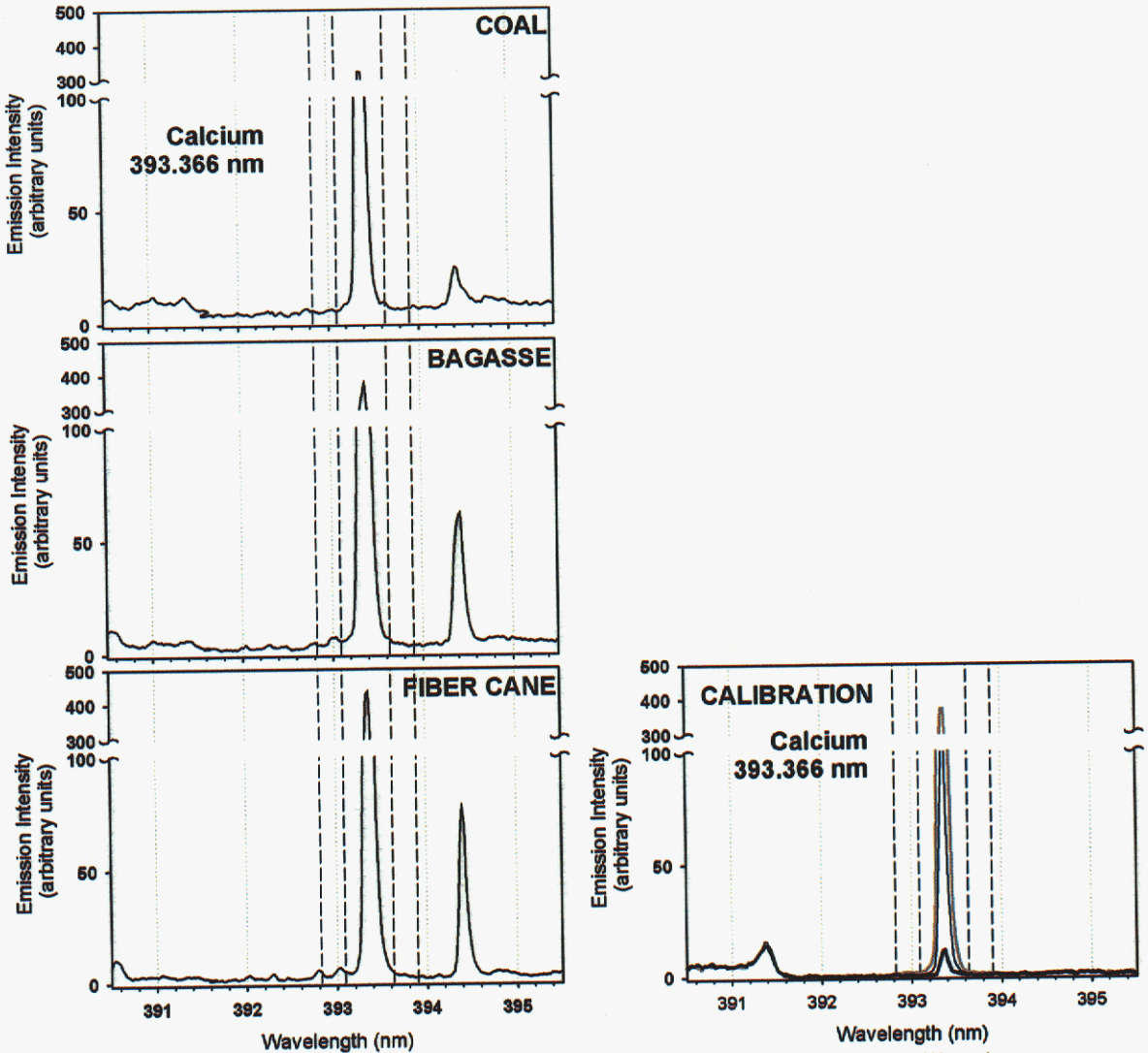

Figure A.5. Calcium signals for the three spectra in Fig. 11 and the three calibration spectra.

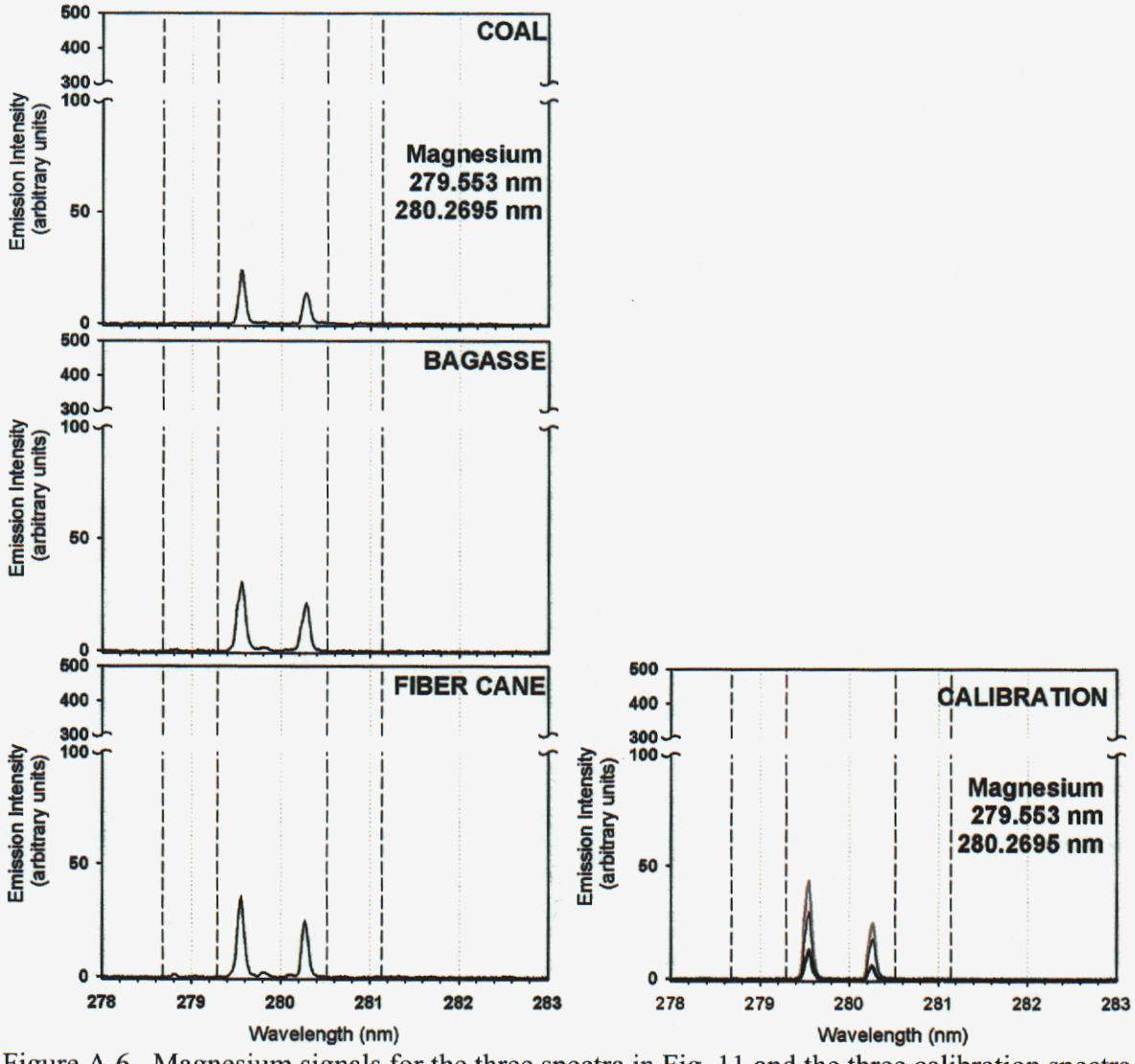

Figure A.6. Magnesium signals for the three spectra in Fig. 11 and the three calibration spectra.

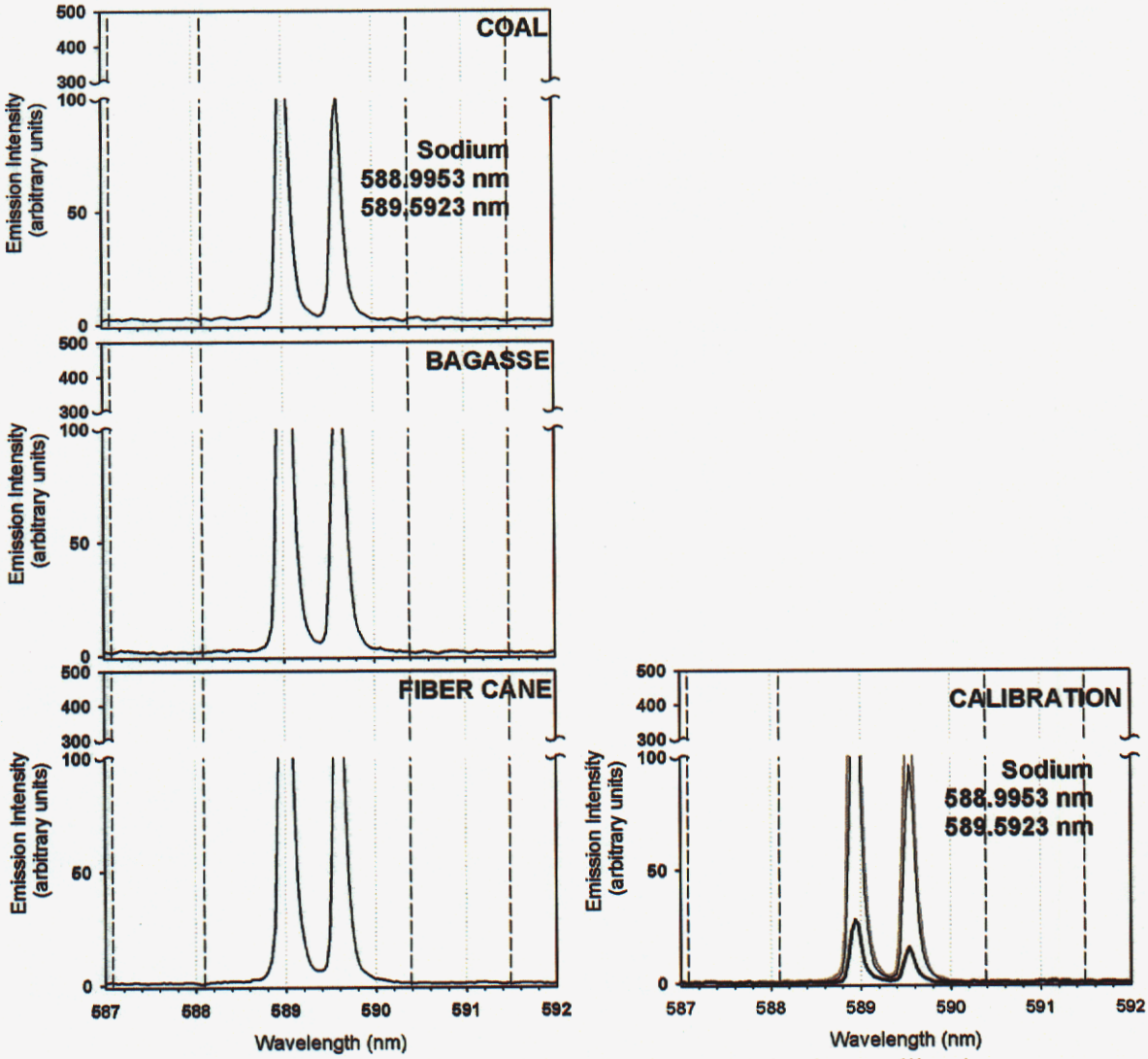

Figure A.7. Sodium signals for the three spectra in Fig. 11 and the three calibration spectra.

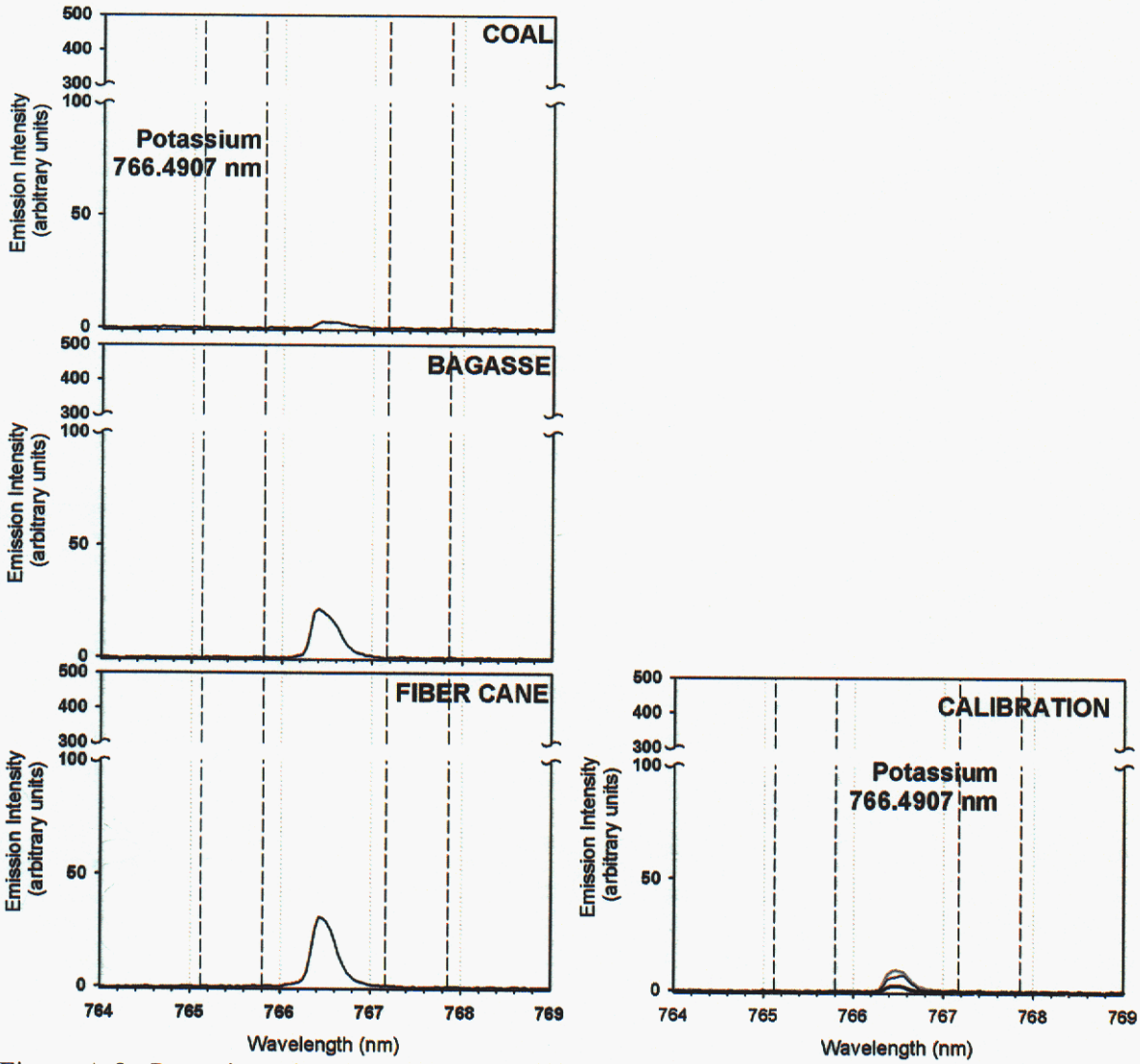

Figure A.8. Potassium signals for the three spectra in Fig. 11 and the three calibration spectra.

APPENDIX B

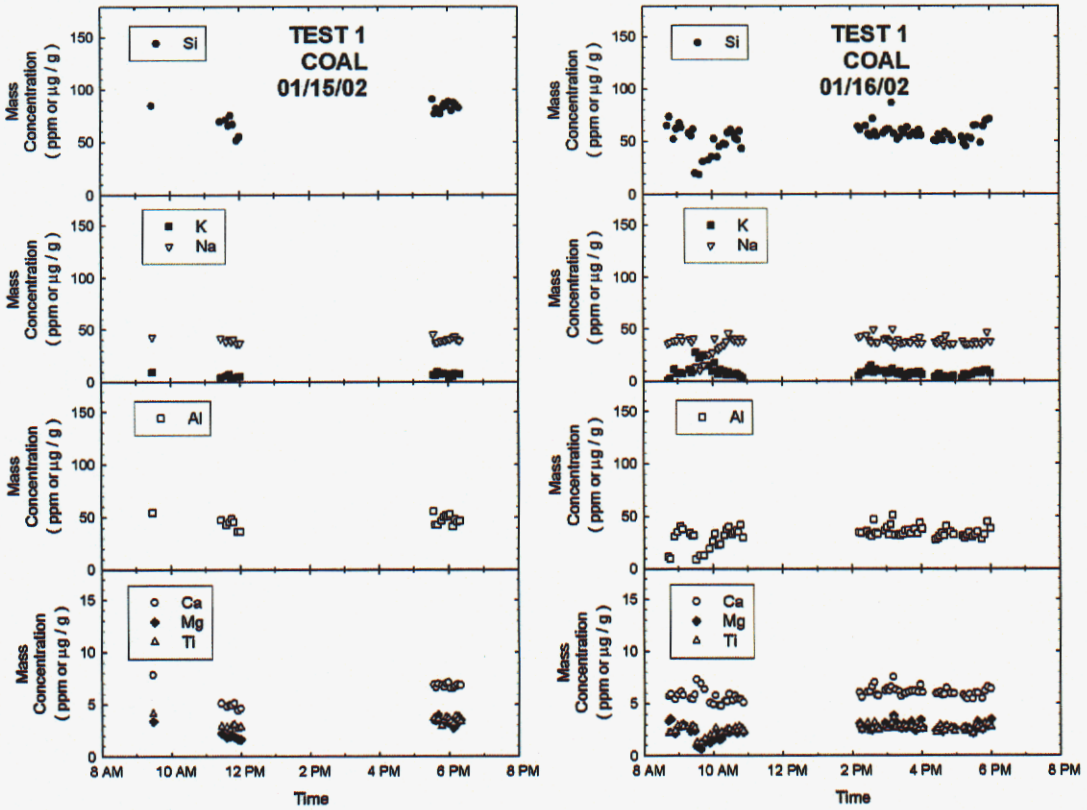

Figure B.1. LIBS-measured concentrations for Jan. 15 and Jan. 16 during Test 1. Spectrometer wavelength calibrations were performed before 8:00 a.m., at 11:40 a.m., at 5:30 p.m., and at 6:30 p.m. on Jan 15; they were performed before 8:00 a.m., at 8:48 a.m., at 9:41 a.m., and at 5:31 p.m. on Jan 16.

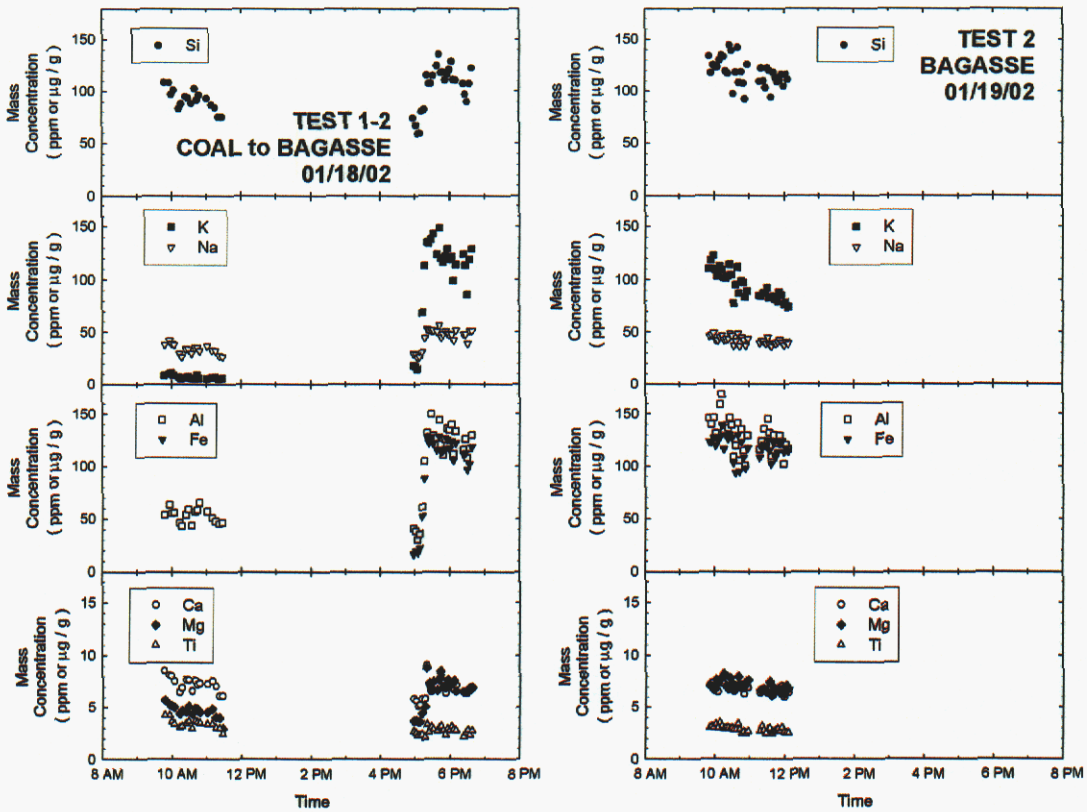

Figure B.2. LIBS-measured concentrations for Jan. 18 during Test 1 (Test 2 after 2 p.m.) and Jan. 16 during Test 1. Spectrometer wavelength calibrations were performed before 8:00 a.m. and at 5:47 p.m. on Jan. 18 (accounting for the increase in signals at that time). A wavelength calibration was performed at 9:35 a.m. on Jan. 19.

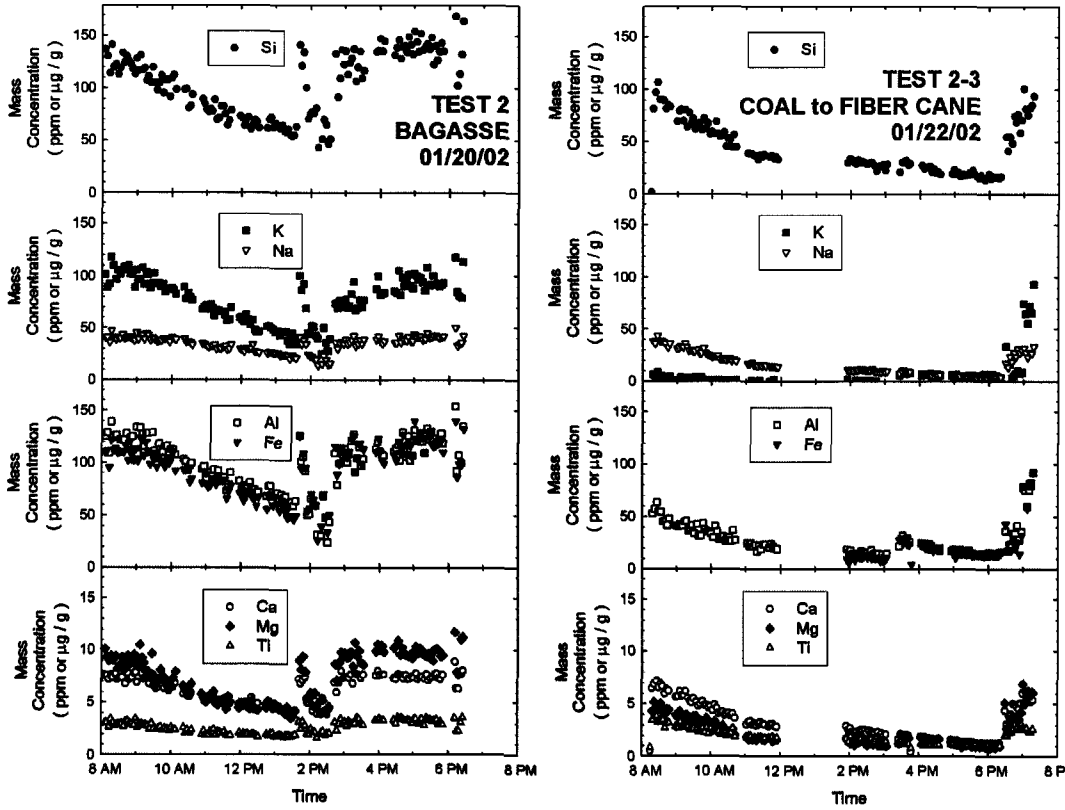

Figure B.3. LIBS-measured concentrations for Jan. 20 during Test 2 and Jan. 22 during the beginning of Test 3 (beginning at 2:00 p.m. with coal burned earlier in the day). Dramatic decreases in signal over time were caused by spectrometer wavelength calibration drift. Spectrometer wavelength calibrations were performed before 8:00 a.m. and 1:36 p.m. on Jan. 20 and before 8:00 a.m. and at 6:23 p.m. on Jan. 22. Data corrupted by spectrometer wavelength calibration drifts were not included in the averages for this report. For all days after Jan. 22, the spectrometer was calibrated for wavelength once per hour.

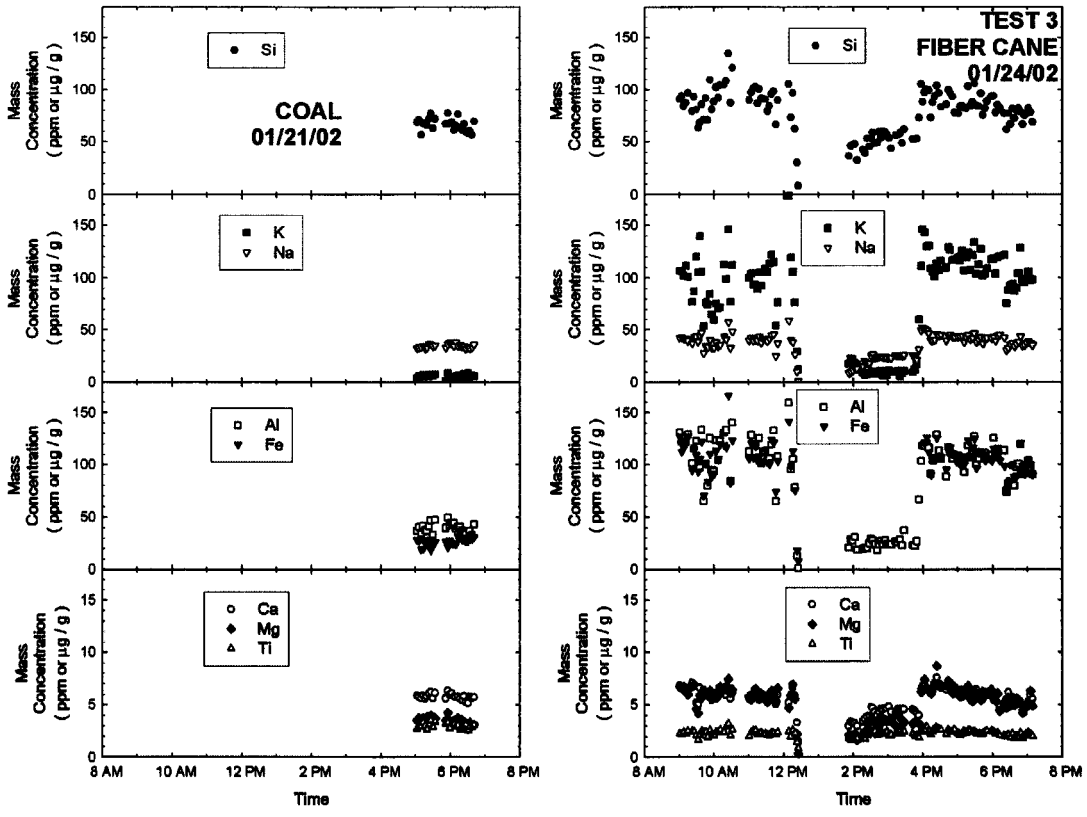

Figure B.4. LIBS-measured concentrations for Jan. 21 (coal only) and Jan. 24 during Test 3. Spectrometer wavelength calibrations were performed once per hour. At about noon on Jan. 24, the boiler was switched from fiber cane co-firing to coal because of biomass feeder malfunctions. At about 4 p.m. on Jan. 24, fiber cane flow into the boiler was restarted. The LIBS signals reflect this fuel switching sequence.

Distribution

Peter M. Walsh
University of Alabama Birmingham
BEC 356F
1530 3rd Avenue S
Birmingham, AL 35294-4461

Lee A. Jakeway
Hawaiian Commercial & Sugar Company
P.O. Box 266
Puunene, Maui, HI 96784

Bryan M. Jenkins
Biological & Agricultural Engineering
University of California
One Shields Avenue
Davis, CA 95616-5294

Robert B. Williams
Biological & Agricultural Engineering
University of California
One Shields Avenue
Davis, CA 95616-5294

Scott Q. Turn
Hawaii Natural Energy Institute
1680 East West Road
Honolulu, HI 96822

James J. Spaeth
U.S. Department of Energy
Golden Field Office
1617 Cole Blvd.
Golden, CO 80401 USA

Paul E. Grabowski
Office of Biomass Programs
EE-2E/Forrestal Building
U.S. Department of Energy
1000 Independence Avenue, S.W.
Washington, DC 20585

Wade A. Amos
National Renewable Energy Laboratory
1617 Cole Boulevard, MS: 1613
Golden, CO 80401-3393

Larry L. Baxter
Chemical Engineering
350 Clyde Building
Brigham Young University
Provo, UT 84602

MS 9052	Jay Keller, Org. 08367
MS 9403	Jim Wang, Org. 08773
MS 9054	Don Hardesty, Org. 08360
MS 9052	Chris Shaddix, Org. 08367
MS 9403	Shane Sickafoose, Org. 08773
MS 9052	Doug Scott, Org. 08367
MS 9221	Gian Sclippa, Org. 08517
MS 9055	Howard Johnsen, Org. 08353
MS 9201	Ben Wu, Org. 08112
MS 9054	Alejandro Molina, Org.08367
MS 9403	Nancy Yang, Org. 08773
MS 9018	Central Technical Files, Org.8945-1 (3 copies)
MS 0899	Technical Library, 9616
MS 9021	Classification Office, 8511 for Technical Library, MS 0899, 9616